Public document

Report of calibration of the tested technologies integrated in the DIGISOIL mapping tool

FP7 – DIGISOIL Project Deliverable D2.3

N° FP7-DIGISOIL-D2.3
March 2010

The DIGISOIL project (FP7-ENV-2007-1 N°211523) is financed by the European Commission under the 7th Framework Programme for Research and Technological Development, Area "Environment", Activity 6.3 "Environmental Technologies".

Geoscience for a sustainable Earth
brgm

Public document

Report of calibration of the tested technologies integrated in the DIGISOIL mapping tool

FP7 – DIGISOIL Project Deliverable D2.3

N° FP7-DIGISOIL-D2.3
March 2010

M. Séger (INRA)
With the collaboration of
I. Cousin (INRA), A. Besson (INRA), R. Mafttei (GIR), F. André (FZJ), S. Lambot (FZJ), J. Thiesson (INRA), F. Garfagnoli (UNIFI), S. Moretti (UNIFI), A. Steevens (UCL), B. van Wesemael (UCL), K. Samyn (BRGM), G. Richard (INRA), G. Grandjean (BRGM)

Checked by:	**Approved by**:
Name: G.Richard	Name: G.Grandjean
Date: 06/03/10	Date: 06/03/10
☑	☑

BRGM's quality management system is certified ISO 9001:2000 by AFAQ.

The DIGISOIL project (FP7-ENV-2007-1 N°211523) is financed by the European Commission under the 7th Framework Programme for Research and Technological Development, Area "Environment", Activity 6.3 "Environmental Technologies".

Geoscience for a sustainable Earth
brgm

Keywords: geophysics, soil properties, field experiments, laboratory experiments, calibration, controlled conditions

In bibliography, this report should be cited as follows:
M. Séger, I. Cousin, A. Besson, R. Mafttei, F. André, S. Lambot, J. Thiesson, F. Garfagnoli, S. Moretti, A. Steevens, B. van Wesemael, K. Samyn, G. Richard, G. Grandjean. 2010. Report of calibration of the tested technologies integrated in the DIGISOIL mapping tool. Report N°BRGM/FP7-DIGISOIL-D2.3; 88 pages.

Synopsis

This deliverable is linked to the second task (2.2) of DIGISOIL's WP2 "Laboratory or field calibration in controlled conditions". The objective here are to report all the experiments that have been conducted under controlled conditions, either in the laboratory, or in the field, both at the calibrating sites Beauce (France), Roujan (France) or Telega (Romania), or in any other field site that has been thought to address a specific soil characteristic. For each geophysical tool, the experimental conditions, the experimental results and the costs of the experiments in terms of man-day are reported.

After a general introduction that indicates the specific content of this deliverable in relationship with the deliverables of WP1 and other deliverables of WP2, each experiment is described in detail. The plan is organized by geophysical tool but several geophysical methods may have been run at the same site. The reader is suggested to refer to Table 9 for synthesis.

Contents

List of illustrations

List of tables

1. Introduction

As mentioned in the WP1 deliverables and the D2.1, the main objectives of the project are to estimate some soil characteristics from geophysical measurements. In this deliverable, we will specifically focus on the measurements of geophysical parameters by geophysical methods, and the measurements of soil characteristics (Figure 1). We remind here that the soil characteristics of interest are the carbon content, the clay content, the water content, and the bulk density. As all these soil characteristics may change with depth due to soil horizonation, a fundamental ancillary data associated with all these soil characteristics is the soil depth.

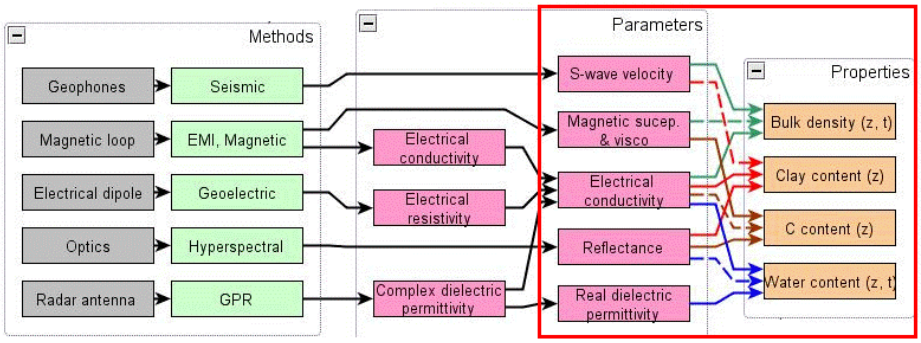

Figure 1: General scheme of the DIGISOIL project to link geophysical measurements to soil characteristics. The red line limits the content of this deliverable, that intends to link geophysical parameters (pink) to soil characteristics (brown).

In the Figure 1, the relationships between geophysical parameters and soil characteristics are represented by arrows. The objective of this deliverable is not to discuss the nature of the arrows, say the processing tools that will be used to link the geophysical parameters to the soil characteristics. This point is discussed in the D2.2 document. We only report here experiments linking geophysical parameters and soil characteristics.

In these studies, geophysical parameters are measured in controlled conditions, i.e. in experimental conditions where the soil characteristics are either controlled or can be easily measured. Depending on the soil characteristics to be measured, the experiments have been conducted in the field or in the laboratory. Some experiments were punctual, when the soil characteristic was supposed to be roughly constant over time, at least at the seasonal scale, like the clay content. Other experiments were time-monitored, when the soil characteristic was supposed to change over time at the seasonal scale; this is the case of i) the soil bulk density, that may change rapidly due to climate effects (developing of cracks due to wetting/drying cycles for example) or to tillage operations, and ii) the water content. Depending on the tillage operations, the

carbon content can or cannot change at the seasonal scale. All these soil characteristics may change with depth.

The following sections describe the geophysical experiments that were conducted in order to link geophysical parameters to soil characteristics. Each paragraph corresponds to a geophysical method, and can be associated to one or more soil parameters. In some cases, several geophysical methods have been used during the same experiment, but the experiment is of course described only once.

The geophysical sensors will not be described in the following, and the reader is suggested to refer to the D1.1, D1.2 and D1.3 to find any useful information about the sensors used for the experiments. The soil characteristics will be usually described by classical tools: TDR probes for the water content, penetrometer for the bulk density, soil sampling and laboratory measurements for the clay content and the carbon content, etc… Except in some specific cases when a particular tool has been used, these methods will not be described neither, and the reader will have to refer to soil physics handbooks to get more information about these measurements systems. The calibration sites – Beauce, Roujan, Telega – will not be described neither in detail, because they have already been presented in the Digisoil DoW document. Only the laboratory experiments and some specific field sites will be described.

2. Geoelectric

2.1. INFLUENCE OF THE SOIL WATER CONTENT AND THE SOIL BULK DENSITY ON ELECTRICAL CONDUCTIVITY MEASUREMENTS: A LABORATORY STUDY

2.1.1. Objectives of the study

The objective was to establish an empirical relationship between electrical conductivity, water content and bulk density. We measured electrical conductivity on disturbed soil cores with known water content and bulk density values. The relation between both soil variables and electrical conductivity is first discussed. Then, an empirical model is suggested. We aim then at developing a conversion model from which the bulk density could be estimated from the geophysical parameter, the influence of all others controlling factors, i.e. temperature and water content, being corrected.

2.1.2. Materials and methods

The studied soil was a Luvisol with a loamy texture (25 g/kg clay, 70 g/kg silt, 5 g/kg sand; Carbon content: 7.8 g/kg) from the INRA experimental site of Mons-en-Chaussée (France). After sampling, the soil was sieved in aggregates (2 mm diameter) and repacked into plastic cylinders (15 cm diameter x 7 cm height). We controlled the water content at repacking in the range 0.08 to 0.25 $g.g^{-1}$ and we made soil cores with a large range of bulk densities, from 1.1 to 1.7 g/cm^3, as commonly encountered in agricultural fields. Once the cylinders were build, their electrical conductivity was measured by a grid of 16 electrodes disposed in 4 lines spaced 4 cm apart (figure 2). The geometry, the location of the electrodes and also the soil volumes measured were chosen in regard to a first methodological work on sensitivity analyze (Richard et al., 2005). The Syscal R1 resistivity meter (IRIS Instruments) was used for the electrical measurements. In parallel, atmospheric temperature was also recorded in view of converting electrical conductivity at reference temperature (Keller and Frischknecht, 1966).

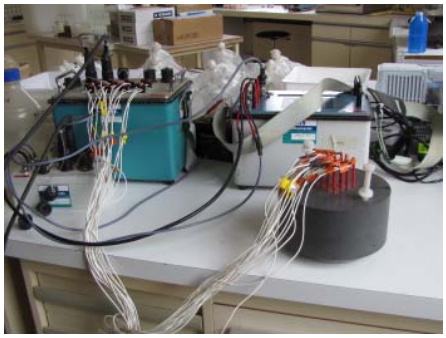

Figure 2: Picture of the experimental device

2.1.3. Results and conclusion

Influence of water content and bulk density on electrical conductivity

Figure 3 presents the electrical conductivity versus the mass water content for the bulk density range analysed.

Whatever bulk density, the electrical conductivity increased when the soil water content increased according to electrolytic conduction in soil (figure 3).

We observe also that the electrical signal depends significantly on the physical property of the soil analysed, i.e. the bulk density. Indeed, the conductivity values are higher when the soil bulk density is high. For instance, the electrical conductivity of soil cores with bulk densities higher than 1.6 g/cm^3 exceeded 30 mS/m. For bulk density closed to 1.1 g/cm^3, the electrical values were smaller than 20 mS/m.

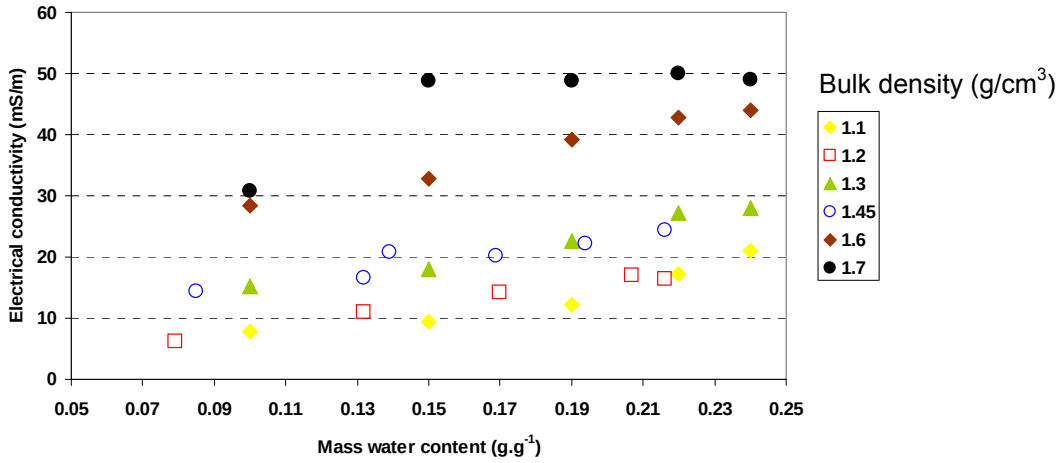

Figure 3: Electrical conductivity versus mass water content for different bul density values (Loamy soil, site of mons-en-Chaussée, France)

Moreover, we observe a threshold in electrical conductivity (approximately equal to 50 mS/m) for soil cores with density value equal to 1.7 g/cm^3 and water content higher than 0.15 g.g^{-1}. This threshold effect could be explained by the changes in the proportion of the microscopic and macroscopic porosity in accordance with bulk density evolution.

These results suggest then the efficiency of electrical conductivity to discriminate the in-field variability of bulk density.

However, the electrical conductivity may depend also on clay content. As shown on figure 3, the values of electrical conductivity for soil cores with bulk density equal to 1.2 and 1.45 g/cm^3 were relatively similar to these measured on the soil cores of 1.3 and 1.45 g/cm^3. This is explained by a small variability in term of clay content between soil cores that can overwhelm, in some extent, the relationship between electrical conductivity and soil bulk density.

Empirical relationship

We determine the best model that represents the relationship between electrical conductivity, water content and bulk density. Regarding the full dataset analyzed by linear regression, we obtain:

$$EC = -66.59 + 52.1\ BD + 110.53\ w \qquad \text{(eq. 1)}$$

where EC is the electrical conductivity (mS.m^{-1}), BD the bulk density (g/cm^3) and w the mass water content (g.g^{-1}). The coefficient of determination is high and significant, equal to 0.901.

This equation (eq. 1) is empirical and is only available for the soil water content and bulk density ranges analyzed.

In regard to the influence of clay content on the electrical conductivity as shown on figure 3, we precise also that the empirical model (eq. 1) cannot be applied whatever soil characteristics.

Conclusions:

- There is a linear relationship between electrical conductivity, mass water content and bulk density in the range of values studied.
- The relationship proposed (eq. 1) is only available for the soil studied and for the water content and the bulk density ranges analysed.
- This methodology is a good one to propose a way to correct the electrical conductivity measured by the effect of water content in view of discussing only the variability in soil bulk density. This methodology could be applied for measuring bulk density from electrical conductivity in field conditions.

2.1.4. Costs of the experiment and experimental difficulties

To be able to produce the same experimentation with the same water content and bulk density ranges, one person need 2 complete months (soil preparation, electrical conductivity and analysis of the results).

This experiment is time-consuming because of drying and sieving. Once a cylinder is prepare, the soil need to be homogenized in term of temperature and hydric state. For that, the soil is put into cold or climatic room during several hours. The preparation and the measurements on one soil sample required about 4 hour.

The water content aimed was never precisely obtained due to evaporation during the preparation of the cylinders. And, for the high values of water content, the soil became difficult to prepare.

The very high bulk density values were difficult to obtain because of the soil mechanical resistance.

2.2. EVOLUTION OF THE ELECTRICAL CONDUCTIVITY WITH BULK DENSITY UNDER NATURAL CONDITIONS: A FIELD EXPERIMENT AT THE BEAUCE SITE

2.2.1. Objectives of the study

The objective was to characterize the structural heterogeneity of the cultivated loamy layer in space and in time at the layer and seasonal scales. We used the non destructive and exhaustive geoelectric method and more precisely the Electrical Resistivity Tomography (ERT) which was proven to be a useful technique for soil structure description (Besson et al., 2004; Séger et al., 2009).

The experiment consisted in space and time in-field monitoring of electrical resistivity (expressed in electrical conductivity) measured on compacted and non compacted soil submitted to drying. The spatial and temporal variability of soil structure in the first layer was then analyzed by 2D ERT comforted by a visual morphological profile.

2.2.2. Materials and methods

Experimental design

The experiment was realized in the Villebon site from the Beauce region (France). The soil was a typical Luvisol that gathersed two main soil layers. The first one was tilled (0-30 cm depth) with textural characteristics of 170 g/kg of clay, 780 g/kg of silt and 50 g/ kg of sand. The second one corresponded to Bt layer according to the clay accumulation process. Its textural characteristic was 205 g kg^{-1} of clay, 750 g/kg of silt and 45 g/kg of sand.

A subplot of 25 m x 7.20 m was chosen for the study (figure 4). We created four compacted bands (Band 1, Band 2, Band 3, Band 4) by wheeling at field capacity (mass water content equal to 23%) with a heavy tractor. This last one enabled high compaction under the wheels. We aimed then at obtaining compacted zones (C) and non-compacted zones (NC).

The studied site was divided in two parts. The first one was cropped (C) with wheat in order to accelerate the drying up of the soil. It was located in the central part of the study plot (figure 4). The wheat crop started in March 2009 and the yield was done in July 2009. After July, the soil was bare in this part. The second one was a bare soil (B) during the entire period of the experiment, located then in borders of the plot.

Consequentially, the experimental design encompassed four modalities: C-C for Compacted and wheat Crop; C-B for Compacted and Bare soil; NC-C for Non-Compacted and wheat Crop and NC-B for Non-Compacted and Bare soil. The soil structure of each band was monitored during 10 months, i.e. from March 2009 (sowing operation) to December 2009. This experimental time gathered three main stages. From March to June, the soil was in wet conditions. From June to October, during the dry period, the soil was dried and cracked. In wetting period, from November to December, the soil was wet according to highest rainfall frequency.

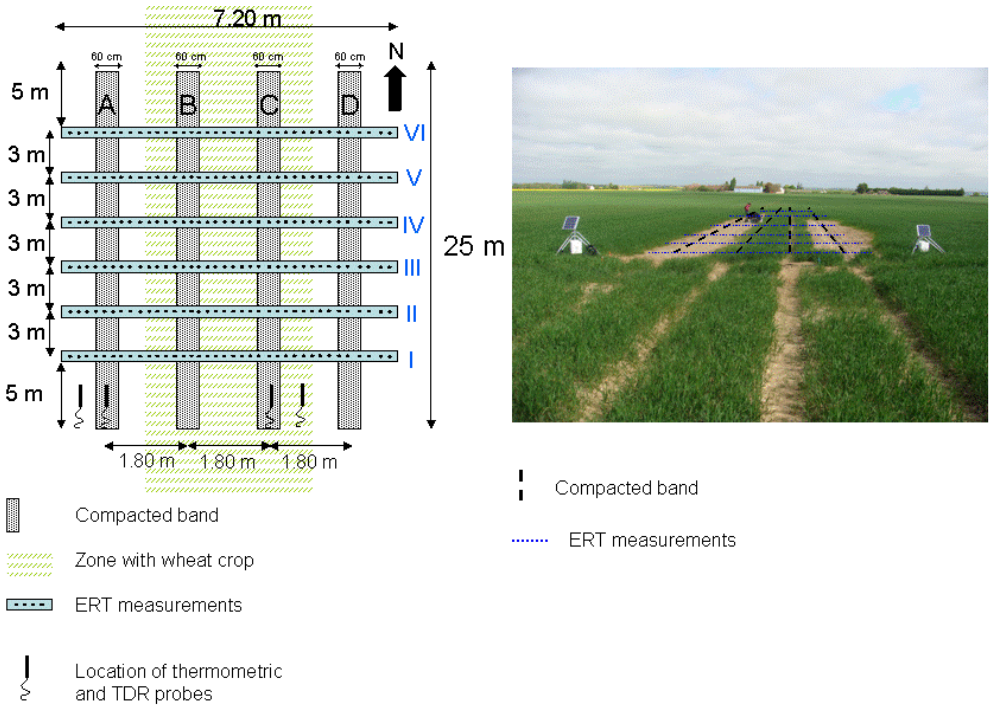

Figure 4: Scheme and picture of the experimental design in the Villebon site. The positions of the compacted bands are located in black and the locations of the ERT sounding are figurate in blue.

Geoelectric measurements

Geoelectrical measurements were realised by a system of 72 electrodes spaced 0.10 m apart (figure 5), switched to a SyscalPro resistivity meter (Iris Instrument). We performed Wenner array acquisitions, as a good compromise noise/resolution, realized along the lines I to VI (figure 4). These lines were perpendicular to the traffic direction.

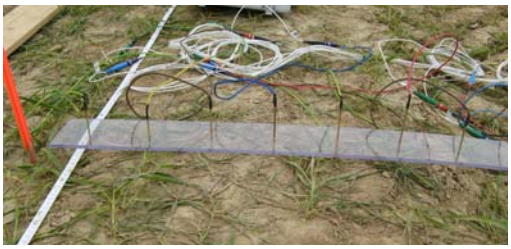

Figure 5: Focus on the system of electrodes used for the ERT measurement

The apparent resistivity data were inverted by the RES2DINV software (Geotomo software). We used the robust inversion (Claerbout and Muir, 1973) where the absolute difference between the measured and calculated apparent resistivity values is minimised. This method, contrary to the conventional least-squares method, reduces the effects of outliers in a very heterogeneous dataset. Inverted electrical resistivity was obtained on refined mesh. In the further, ERT results will be expressed in electrical conductivity, i.e. the inverse opposite of resistivity. They will be then also named ECT for Electrical Conductivity Tomography.

Because of their influences on electrical conductivity, the soil temperature and the volumetric water content were recorded during the experiment. They were measured hourly by respectively thermometric probes and TDR probes (Topp et al. 1980) during experiments. The probes were installed from 5 cm to 55 cm depth for non-compacted zones (modalities NC-C and NC-B) and from 15 cm to 55 cm depth for compacted bands (modalities C-C and C-B). Their locations were sufficiently close to ERT positions for comparison whit ERT results, but far enough to avoid sensors interactions. The impact of temperature on electrical measurements was also corrected by the use of Keller and Frischknecht equation (1966).

Visual morphological descriptions

For all modalities, i.e. C-C, C-B, NC-C, NC-B, the soil structure was visually described on soil pits dug in the field at the similar locations of ECT, i.e. along the lines I to VI. The visual description was realized by the morphological method as described by Roger-Estrade et al. (2004). Within this method, the soil zones showing different degrees of compaction were then delineated.

Additionally, bulk density and water content values were measured on undisturbed soil cores sampled in different zones delineated on soil profiles. Measurements were done for all modalities at 5, 15, 25 and 35 cm depth for the non-compacted zones and at 15, 25 and 35 cm depth for the compacted zones.

Spatial and temporal monitoring of the soil structure

ECT measurements were then realized all along the lines I to IV. They covered then the cropping system as well bare soils, compacted or not. They gave a description in 2D of soil with an investigated depth close to 80 cm. ECT monitoring was realized twice a week and sometimes twice a month from March 2009 to December 2009.

In parallel visual morphological descriptions of the soil structure and soil sampling were realized on soil pits dug at the similar position of ECT and after ECT acquisition. We aimed here at comforting ECT interpretation in term of soil structural heterogeneity. The method is destructive and could be realized only once. In addition, it is evident that ECT monitoring on a line could not be carried on once the soil pit dug. As a results only four visual descriptions corresponding to lines I to IV were then realized, i.e; in June for line VI, in July for line V, in August for line IV and in November for line III. We assumed that the soil structure variability visually described at a date and for one line (I to IV) was representative of the studied area in regard to modalities.

In the next section, the line III will be analysed. We show and discuss the results on water content and bulk density obtained on soil core at three dates for line.

2.2.3. Results and conclusions

Soil structure at the start of experiment as described by destructive methods

Large compacted zones (0.60 m x 0.30 m) were visually identified on soil pits at the position of the wheel tracks ways. Figure 6 presents an example of observation of a compacted zone under wheel track.

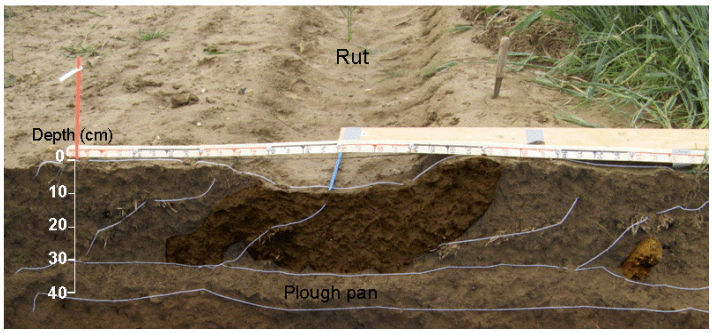

Figure 6: Compacted zone under wheel track. The shaded zones represent the soil with a high degree of compaction (no visible porosity). The white lines represent the position of the plough pan and the limits between adjacent furrows.

Mean value of bulk density measured on soil cores sampled in these compacted zones was equal to 1.55 g.cm^{-3} whereas the mean bulk density of non-compacted zones was approximately equal to 1.35 g.cm^{-3}. Difference in mean values is significant.

Interpretation of Electrical Conductivity Tomographies in term of soil structure

Figure 7 shows results on ECT after correction on the temperature effect. ECT were measured at the same location (line III, figure 4) at the three dates in June, August and November. Compacted bands, cropping system and bare soil are also located for a best understanding. The volume water content profiles are represented for each date on the right side of the ECT.

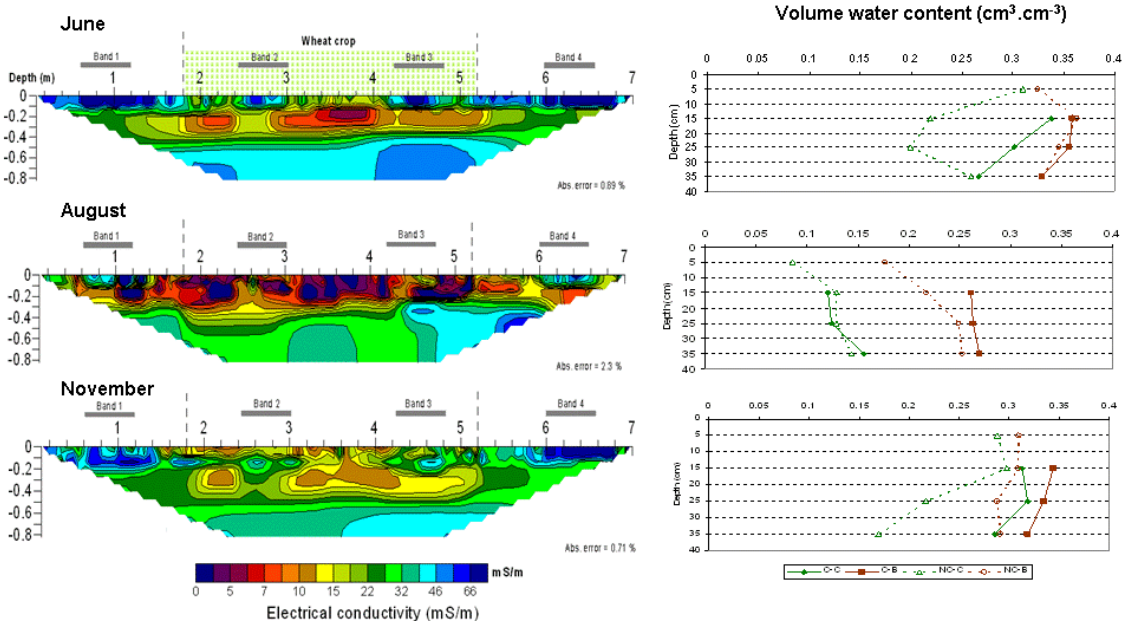

Figure 7: 2D Electrical Conductivity tomographies obtained on line III and at three dates and the volume water content profiles corresponding. The reference depth is the soil surface for NC zones

Three main patterns can be observed on ECT, (1) a first geophysical layer in the near surface, i.e. in the ten top centimetres of soil, which presents a strong variability in electrical conductivity, (2) an intermediate layer that corresponds to the bottom of the tilled layer and the transition between soil horizons, with small values of conductivity and (3) a third layer corresponding to Bt horizon with high conductivity in accordance with higher clay content.

In the further we discussed only on results obtained in the tilled layer more subjected to structural variability imposed by the experimental protocol. Tilled layer gathers approximately the two first geophysical layers as mentioned above.

In June, results of ECT enable to identify and to locate in space compacted bands with electrical conductivity values ranging from 40 to 65 mS/m. These values are relatively high in near surface. They may be explained by the high bulk density of compacted clods. Indeed as yet described in chapter 2.1 of this deliverable, the correlation between both variables is high and significant. The electrical conductivity increases with bulk density. However the characterization of compacted bands is more evident in

baresoils (bands 1 and 4) than in the cropping system (bands 2 and 3). The cumulative effect of soil water content overwhelms the identification of compacted clods by ECT. This appears particularly in baresoil where the soil water content in near surface is relatively high. The electrical conductivity increases with soil water content as well as bulk density. As a result the contrast in electrical conductivity related only to compaction is attenuate in wet bare soil. Reversely, when the soil water content in the cropping system is smallest according to the root water uptake, compacted clods in this zone can be easily identified by high values of conductivity surrounding in a matrix generally resistant.

Between 10 cm to 40 m depth, the electrical conductivity is relatively homogeneous with small values according to the loam content. ECT shows, nevertheless, zones with values of conductivity sensibly highest under compacted bands. This may be explained by the umbrella effect in the inversion process related the conductive anomalies obtained in the near surface. Additionally, the plough pan as described on visual morphological profile is not distinguished on ECT. As for water content effect, the influence of clay content on electrical conductivity can overwhelm the presence of plough pan.

In August, the full tilled layer is characterized by very small values of electrical conductivity. The decrease in water content in the tilled layer and also on the entire soil profile can explain small values. Soil cracking is also prominent in August. Cracks represent structural components particularly resistant. In addition, they create noise in electrical measurements and then restrict the inversion process.

In November, compacted bands are hardly identified on ECT in the cultivated zone. They may have been disaggregated during the cropping season. The tilled layer shows values of electrical conductivity relatively small, probably due to the presence of crop residues. In addition we observe highest values of conductivity in baresoil in accordance with the highest water content in the tilled horizon. Probably as a result of the soil natural consolidation in baresoil, water infiltration can be restricted. Reversely, the tilled layer is strongly disturbed and disaggregated in cropping system. It encompasses numerous preferential flow paths such as wormholes, interraggregate cracks, large voids and macropores. Enhanced preferential water flow directed towards the incorporated straw can also occur.

- *To conclude and for further work:*

  The geoelectric method is sufficiently sensible to locate and characterize in space and time the variability of the soil structure. We have given first results and discussed on them. Further works will be realised in view of:

  - testing different schemes of inversion to reduce noise effect on electrical estimates,
  - validating ECT from pictures of the morphological profiles realized,

- elaborating an empirical conversion model adapted to the soil conditions of Villebon site experiment. From laboratory experiments, the relation between electrical conductivity, water content and bulk density. We should be then able to correct ECT measurements from water content effect and finally to obtain 2D profile of the bulk density.

2.2.4. Costs of the experiment and experimental difficulties

The geometry of the geoelectrical device and the electrodes configuration must be adapted to topics investigated. Knowledge on the ratio noise/resolution is required in considerations to the main objective of experiments.

The electrodes spacing of the geoelectical device should be relatively close to the size of compacted zones, i.e. at the decimetric scale. The exact spacing between electrodes and the linearity of the device should be respected carefully. Indeed this can have a drastic impact on precision of measurements. For further works realized at the field scale, we suggest then to adapt the geoelectric MUCEP device with smaller inter-electrode spacing.

The soil/electrode contact was sometime difficult to stabilize especially during the dry period. Often a small quantity of water was then added at the base of electrodes to facilitate the electrical contact.

In view of describing the soil structure in space, it seems crucial to perform the geoelectric method at the start of desiccation period. We have shown, effectively, that the contrast in electrical conductivity obtained at this period is easier to interpret in term of structural variability.

The field work requested 3 persons for the electrical measurements and 5 for the soil morphological profiles. The number of person-day needed for the field work was 105.

The dataset is important and required two persons fully occupied for treatments.

2.3. MONITORING SHALLOW LANDSLIDES AT TELEGA SITE

2.3.1. Objectives

Objectives are here related to testing of several types of arrays and intervals between measurement points in order to find the best investigative methodology to characterize landslides.

2.3.2. Material and methods

Experimental site

The studied site was chosen because of its shallow landslides caused by the salt deposits presence. Also, the access in the area is very easy, so the tests can be made without any problems.

The soils in this area are argilaceous and salty. They are strongly eroded. The Telega baths are situated around salted lakes which are in the NW part of the Telega commune, at the “Butoi” zone. The access is available from the Telega-Melicesti road. The deposits which occur in these areas belong to the evaporitic formation of Middle Miocene-Badenian age. Also, near the rivulet, salt occurrences are observed. The slopes are rather steep, especially near the ridge. The upper part of the slope is occupied by orchards (or what is left of them as a result of landslides) and pastures belonging to the locals. The scarps have semicircle or irregular forms. The landslides are present on the left side of the Telega Valley, reaching near to the summit of the hill and to the road to Bustenari. On the slided mass, frequent longitudinal and transversal cracks are observed, a lot of them with water accumulations. They have variable dimensions: breadths between 5-30 cm, depths around 10-120 cm. At this moment we consider that the landslide has three parts. The initial scarp, situated near the hill’s ridge, has an amphitheater aspect. We have estimated it’s height around 20 m. At the base of the scarp there are accumulations of randomly disposed argillaceous sand blocks.

In the spring of year 2000, as a result of very important rainfall, new profound and shallow slidings were produced affecting the pasture and some fences which limit the locals' properties. These are the second and third parts of the landslide. The stakes of the broken fences were moved and dragged on a 5-6 m distance. These landslides are typical of the phenomena which affect the slopes made of salty deposits. Also, the fact that the infiltration waters can be in direct contact with the argillaceous cement of the salt breccias can lead to the overlapped deposits displacement on the slope.

Experimental device

Our experiment consists in carrying out geoelectrical investigations in resistivity imaging version, on a longitudinal profile L and 5 transversal profiles T0 - T4, uniformly covering the largest part of area affected by landslide. The geophysical device encompassed SuperSting R8/IP+64 automatic resistivity and IP system, with built-in central switching for 64 electrodes and passive multielectrode cables.

In the first stage, the longitudinal profile and the 5 cross profiles were measured with 5 m spacing using 4 array types:

- Schlumberger1 array with Max AB/MN = 10 and expansion factor = 7 (figure 8);

- Schlumberger2 array with Max AB/MN = 20 and expansion factor = 6 (figure 9);

- Wenner array with expansion factor = 7 (figure 10);

- dipole-dipole array with Max n = 2 (figure 11).

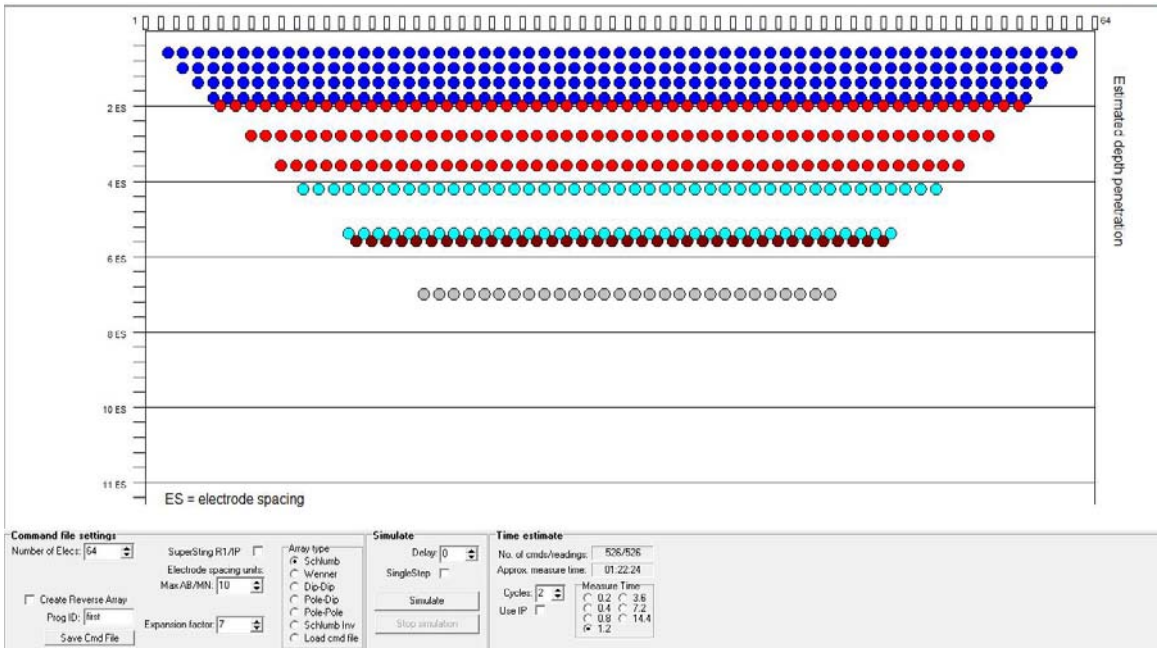

Figure 8: Sequence performed with the Schlumberger1 array

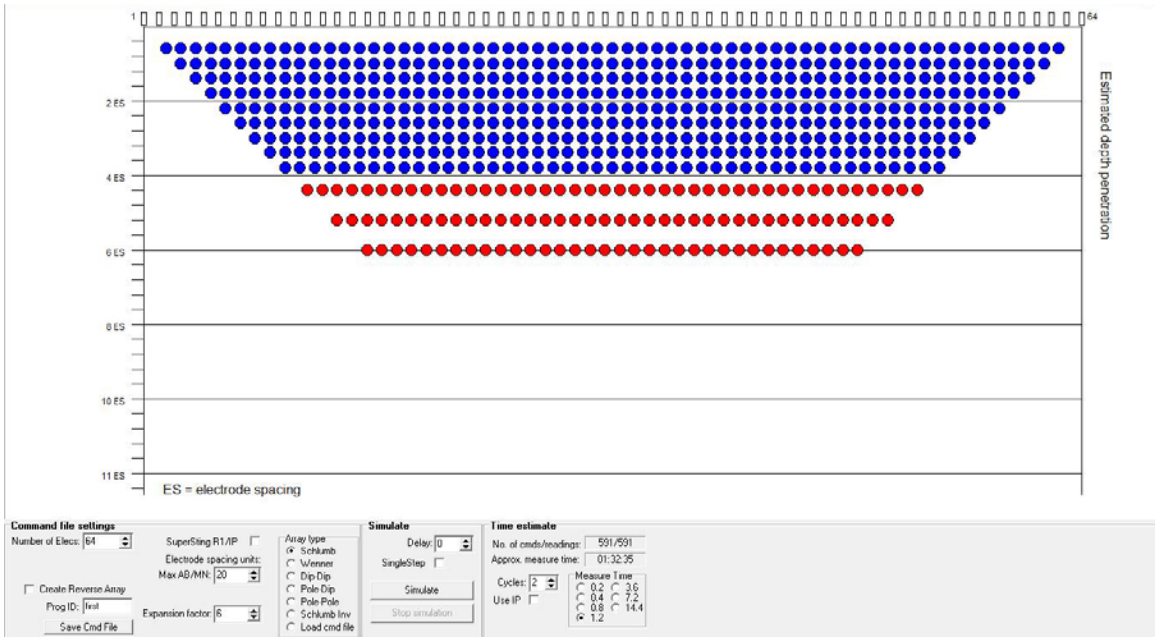

Figure 9: Sequence performed with the Schlumberger2 array

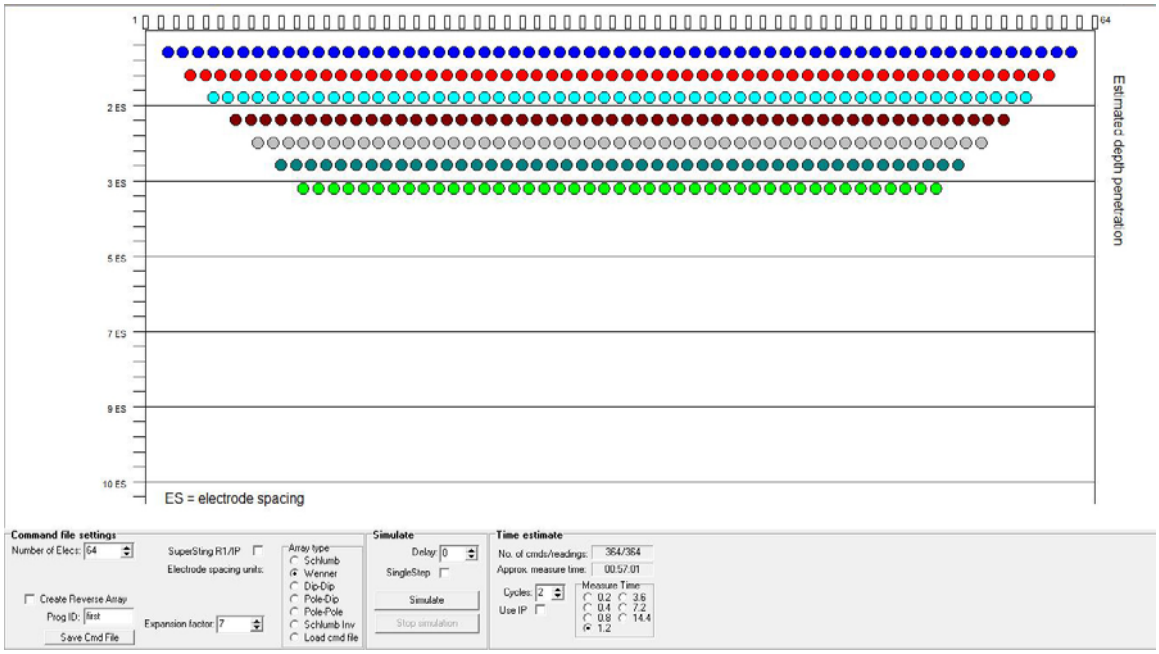

Figure 10: Sequence perforemed with the Wenner array

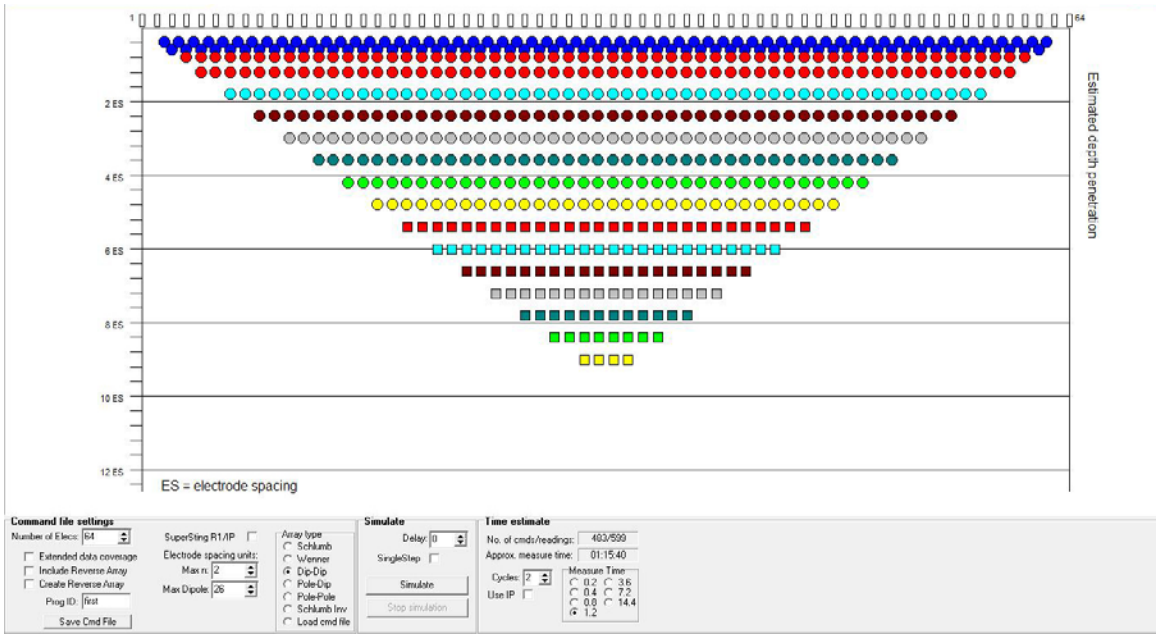

Figure 11: Sequence performed with the dipole-dipole array

In the second stage, the higher part of longitudinal profile and the transversal profile T2 were measured with the Schlumberger array determined from these tests as having the

best resolution and ability to differentiate various components of sliding, using two intervals between soundings, 5 and 2.5 m.

2.3.3. Results and conclusions

Figure 12 presents the inverted resistivity section for the L-profile and for 3 arrays: Schlumberger1, Schlumberger2 and Wenner.

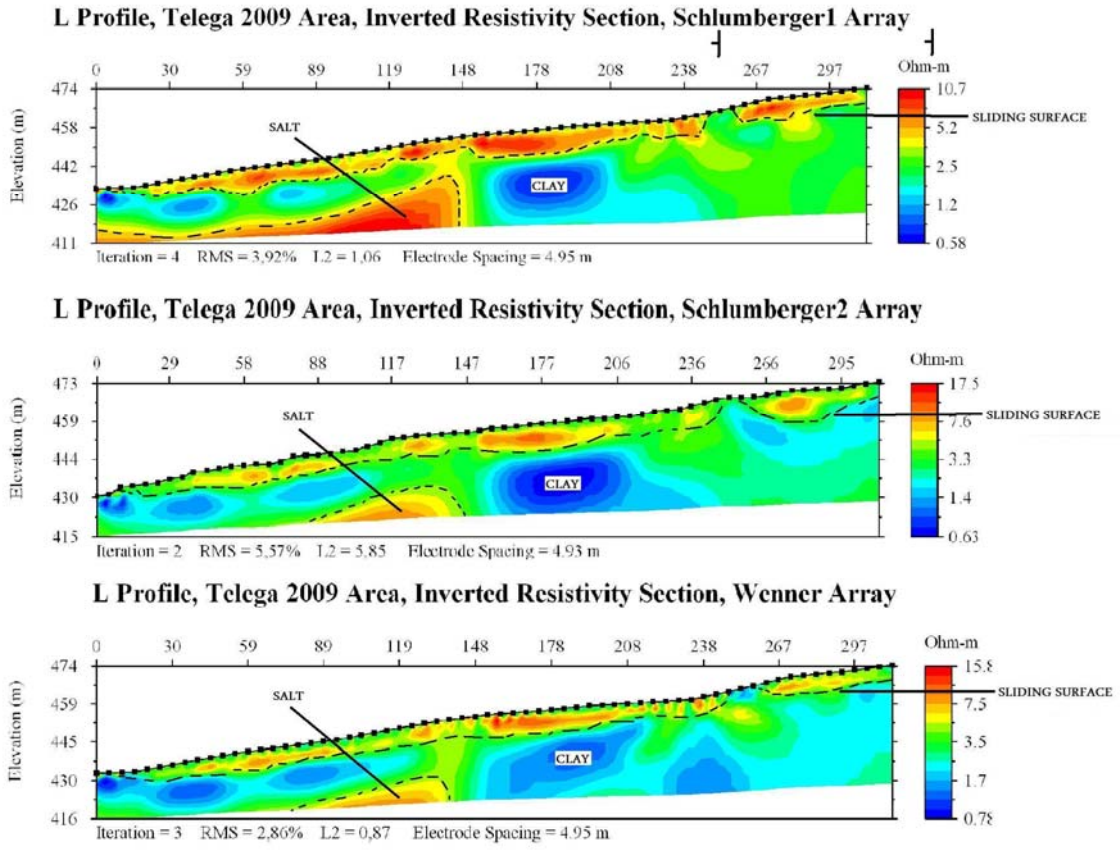

Figure 12: Inverted resistivity section obtained on the longitudinal profile for the Schlumberger1 array, the Schlumberger2 array and the Wenner array

Results show that:

- A greater spacing between measurement points (5 m) allows obtaining a deep investigation of the subsoil up to 30 - 40 m, a general resistivimetric image, an overall plan of the internal structure of the landslide. Sliding surface and component parts on the landslide was outlined more clearly, due to high resistivity contrast between them.

- A smaller spacing (2.5 m) allows obtaining a detailed image of subsoil resistivity distribution. The smaller depth of investigation is sufficient to contour the upper sliding surfaces, usually active, located up to 20 m deep, but is sometimes insufficient to investigate possible deep sliding surfaces, probably temporarily stabilized.

- To obtain suggestive results, measurements should be made with two different spacing between measurement points, in order to obtain a high resistivity resolution in subsurface and for deepest layers.

- The dipole-dipole measurements are the fastest and have a good lateral resolution. However, the signal looses quickly and inverted resistivity images reveal a large RMS error and are not suggestive. It is recommended to investigate some simple structures, but inappropriate for landslides.

- The Wenner array supposes a longer measurement time, the signal is strong, RMS errors are small, but produces low contrast and less details images.

- The Schlumberger array supposes a longer measurement time, but have a good signal strength and produces sharp and suggestive images, with many details of the resistivity distribution. RMS errors are quite small, within acceptable limits, usually below 4-5%. It is the most appropriate array type to apply in the case of very complicated geological structures, such as most landslides.

2.3.4. Costs of the experiment and experimental difficulties

The approximate cost in terms of person-day for that field experiment was about 28 days with 3 persons resulting in total in 3 person.month. The soil-electrode contact was sometime difficult to stabilize especially during the dry period.

3. Electromagnetic induction and Ground Penetrating Radar

3.1. DETERMINATION OF SPATIAL AND TEMPORAL VARIATION OF SOIL WATER CONTENT AT THE FIELD SCALE

3.1.1. Objectives of the study

The objective was to investigate the spatial and temporal variation of soil water content in the field using ground penetrating radar (GPR) and electromagnetic induction (EMI) and to compare soil water content estimations from both techniques with TDR estimates used as references. For spatial analysis of soil water content, irrigation was applied prior to the measurements with contrasted intensities on different areas of the study site, so as to cover a wide range of soil water contents. For temporal analysis, soil moisture variations were monitored with GPR and TDR at a single location over a period of 25 days.

3.1.2. Materials and methods

The experiment was conducted on 14th July 2009 at the Selhausen test site, situated in the southern part of the Lower Rhine Embayment in Germany (longitude 50°87 N, latitude 6°45E, 105 m elevation above sea level), on a field plot of 1.33 ha. The test site is weakly inclined (slope < 4°) in the east-west direction. The ground water depth shows seasonal fluctuations between 3 m and 5 m below the surface. The soil has been developed from Quaternary sediments, which are mostly fluvial deposits from the Rhine/Meuse river and the Rur river system, covered by eolian sediments (up to a depth of 1 m) from the Pleistocene and Holocene. According to the USDA textural classification, the soil type is a Haplic Luvisol developed in silt loam. The first 30 cm of the soil contain 35% sand, 52% silt, and 13% clay (Weihermüller et al., 2007).

For the spatial soil water content analysis, GPR, EMI and TDR measurements were carried out at identical positions arranged on a 68 m $\times$ 14 m grid in the upper part of the site: 18 measurements were performed every 4 meters along 8 transects separated each by 2 meters. Some parts of the study area were irrigated prior to the measurements, thereby providing three distinct water content ranges (figure 13): ‘control’ (natural water content), ‘intermediate’ (natural + 4 mm irrigation), and ‘high’ (natural + 8 mm irrigation). In addition, GPR and TDR measurements were also carried out every 4 meters along a 100 m transect in an area where natural variation of surface soil water content was observed.

GPR measurements were performed using the off-ground frequency domain GPR prototype developed by UCL and FZJ at 301 stepped frequencies over the range 0.2-2 GHz with a frequency step of 6 MHz. However, only the lower frequencies, between 0.2 and 0.8 GHz, were used for the inversions in order to avoid the influence of soil roughness on the data. EMI measurements were carried out both in vertical and horizontal dipole modes using the EM38 (Geonics), operating at 14.6 kHz, and the EMP-400 Profiler (GSSI) for which the 5 kHz, 10 kHz and 15 kHz operating frequencies were selected. TDR measurements were performed at four juxtaposed locations within the GPR antenna footprint using a custom-made 10 cm length three-rod probe inserted vertically into the soil and connected to a TDR100 cable tester (Campbell Scientific, Logan, UT). For the time-lapse monitoring experiment, the GPR setup was the same as presented above for the spatial analysis and two TDR probes were installed 1 meter apart from each other at 8 cm depth nearby the GPR antenna footprint. Both TDR and GPR measurements were carried out with a time-step of 15 min for 25 days during summer 2009.

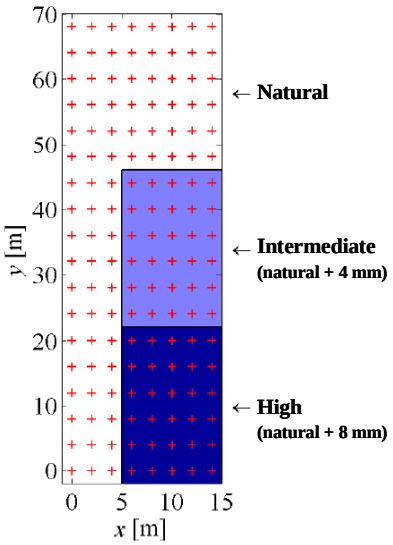

Figure 13: Diagram of the measurement grid and location of water content levels at the Selhausen test site

3.1.3. Results and conclusion

Maps of GPR and TDR dielectric permittivity measurements and corresponding estimates of soil water content using the Topp et al. (1980) equation are shown in figure 14. Similarly, figure 15 presents maps of soil electrical conductivity determined with the EM38 and Profiler in both horizontal and vertical dipole modes and the corresponding soil water content estimations using Archie's equation modified by Shah and Singh (2005). In each case, gradients of dielectric permittivity, of electrical conductivity and of water content estimates are observed and are in rather good correspondence with irrigation levels. Good agreement is observed between GPR and TDR water content estimates (figures 14, 16 and 17)

as these techniques have comparable investigation depths, i.e., the upper 3-10 cm of the soil. Estimations of soil water content from horizontal dipole EMI measurements tend to be somewhat lower than GPR and TDR estimates, while vertical dipole measurements provide much higher water content estimations compared with TDR and GPR. These differences might arise from several reasons. First, investigation depths of EMI is around 0.70-0.80 m and 1.50-1.80 m for horizontal and vertical dipole orientations, respectively, which is much higher than characterization depths of TDR and GPR. Generally lower water content estimates from horizontal dipole EMI measurements would result from the fact that irrigation was only applied some hours before the measurements and the sprayed water did not have time to infiltrate. In contrast, high water content estimated from vertical dipole measurements would indicate the presence of humid soil layers at lower depth. Differences amongst methods could also partly arise from the parameterization from the equations used to convert soil dielectric permittivity and electrical permittivity, which should ideally be calibrated for the study site. A supplementary explanation for the differences could be related to the major limitation of the EMI commercial sensors we used, which classical calibration procedure is inaccurate and not easily repeatable. In that respect, we are currently working on the development of a new methodology for a more robust calibration of these sensors. Comparing EMI measurements, results from EM38 are similar to those of the Profiler at 10 kHz and 15 kHz, while data from Profiler at 5 kHz show much stronger spatial variations, which could at least partly result from a greater influence of the environment (other sensors and probes installed at the study site) at that frequency compared with the others. A general decrease of soil water content estimated from GPR and TDR is observed along the 100 m transect, with generally good agreement between both techniques (figure 17). At each location, variation of water content of 2-7% was observed in the 95% confidence interval of the TDR measurements, which results from local soil heterogeneity.

Results for the time-lapse experiment are presented in figure 18. The three major peaks in the data correspond to the three major rain events that occurred during the measurements. Differences are observed between water contents inferred by the two TDR probes, especially after the rain events. Such observations would result from lateral variations of soil hydraulic properties due to local soil heterogeneities. After each rain event, soil water contents estimated with GPR were higher than estimations from TDR. These differences between GPR and TDR arise from the fact that GPR is sensitive to the surface soil water content (≈ 0-5 cm) while TDR probes were located at 8 cm depth. During the dry periods, the surface soil water content steadily decreased as a result of evaporation, which was well observed by GPR.

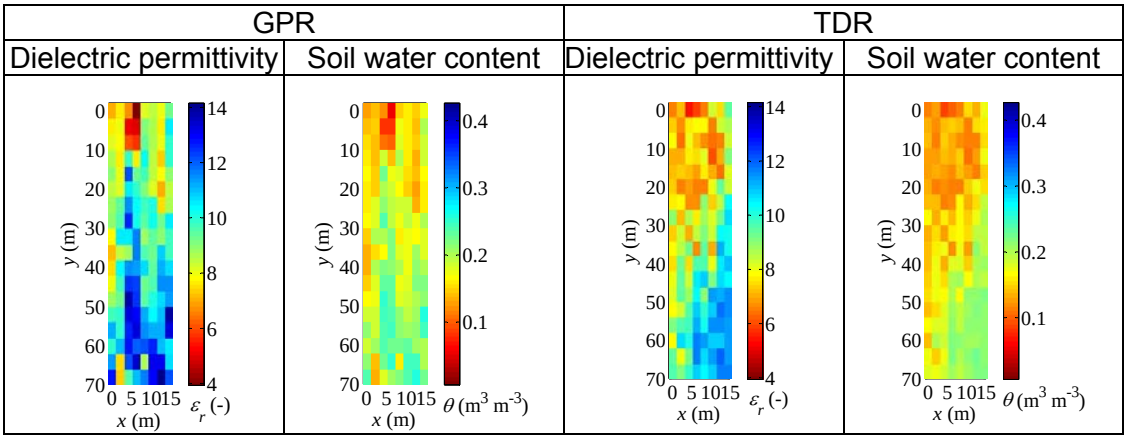

Figure 14: Measurements of dielectric permittivity with TDR probes and water content estimates at the Selhausen test site

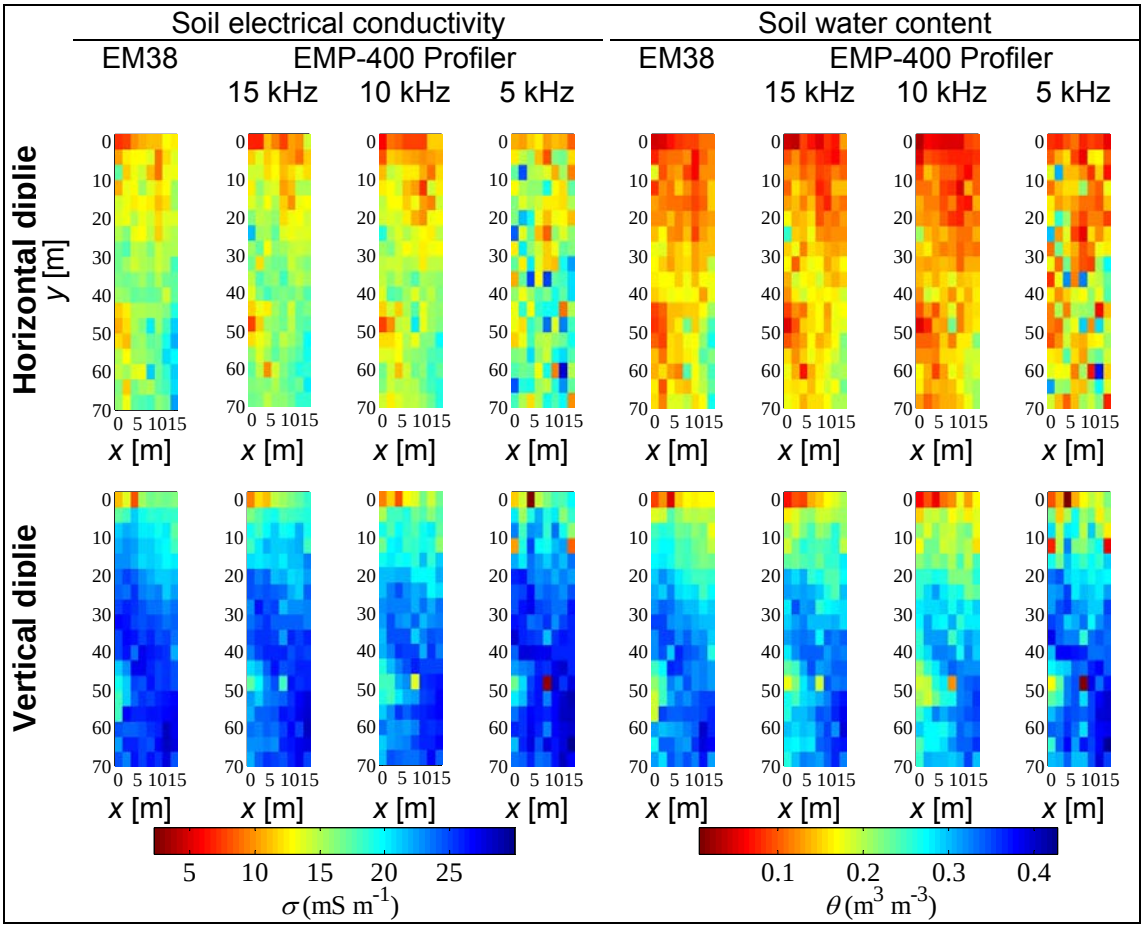

Figure 15: Measurements of electrical conductivity with the EM38 and EMP-400 Profiler and water content estimates for the irrigation experiment

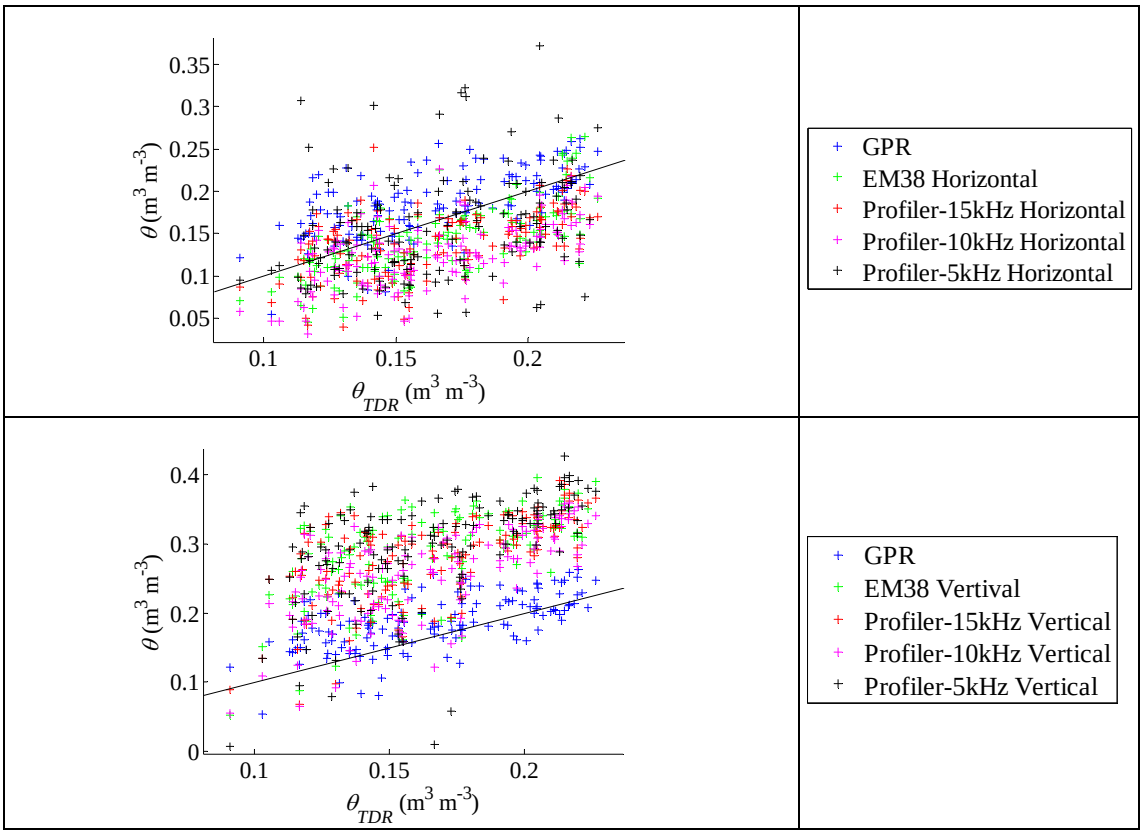

Figure 16: Comparison of GPR and EMI and TDR water content estimates for the irrigation experiment (the black line is the 1:1 line)

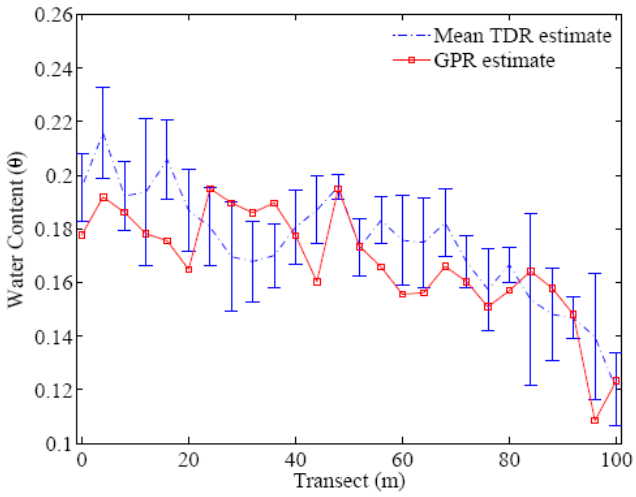

Figure 17: Comparison of GPR and TDR measurements along one transect of the irrigation experiment (error bars are 95% confidence intervals from the 4 replicates)

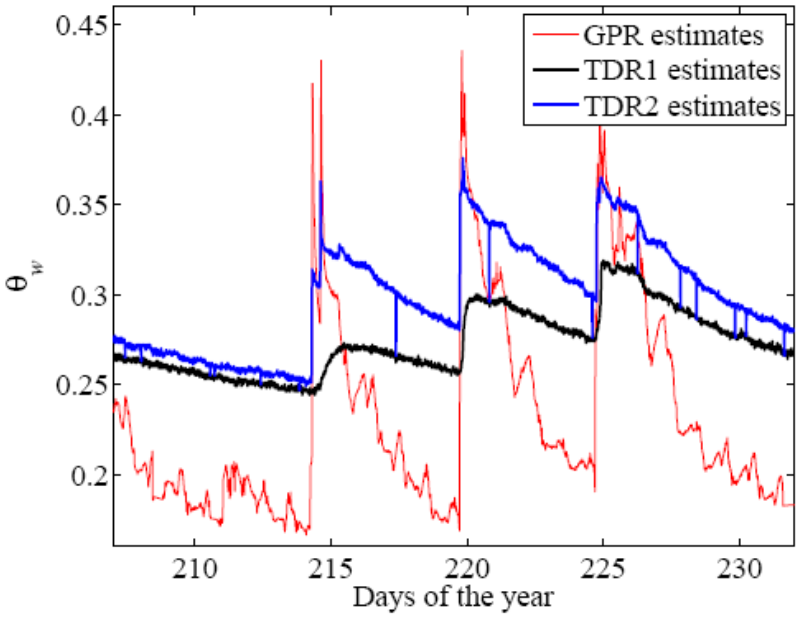

Figure 18: Estimated water content by using two TDR probes, installed horizontally at 8 cm depth within the foot-print of GPR antenna and the water content inferred from GPR signal.

3.1.4. Costs of the experiment and experimental difficulties

The approximate cost in terms of person-day for that field experiment was about 6 for the mapping plus 4 for the time-lapse measurements (semi-automated), resulting in total in 10 person-days.

3.2. SURFACE SOIL WATER CONTENT ESTIMATION BY GPR IN THE PRESENCE OF THIN LAYERS

3.2.1. Objectives of the study

The objective was to analyze the effect of shallow thin layers on the estimation of soil surface water content using full-waveform inversion of GPR data. Strong vertical dielectric contrasts that are expected to occur under natural conditions may lead to constructive and destructive interferences with respect to the surface reflection. Laboratory experiments were performed to assess the capabilities of a two-layered model to retrieve the surface soil water content in the presence of thin layering in controlled conditions. Then, the method was tested with field data.

3.2.2. Materials and methods

For the laboratory experiment, a square box was filled with two layers of sand with different water contents. The top thin layer was subject to 10 different water contents, ranging from 0 to 0.270 and to 5 different thicknesses, whereas the second layer properties were kept constant, resulting in total in 50 different configurations. GPR measurements were acquired with the antenna suspended above the sand surface at 301 stepped frequencies in the frequency range 800-2600 MHz and subsequently inverted assuming a two-layered model. Sand water content was measured by volumetric sampling as a ground truth.

The field acquisition took place on the 23th of March 2009 in an 11-ha cultivated field located in the center of Belgium (Long. 4°41'8"E, Lat. 50°35'59"N). Soil type is uniformly a silt loam, with a gentle topography ranging from 153 to 161 m a.s.l and slope lower than 7%. A total of 3741 GPR measurements were acquired at 301 stepped frequencies from 200 to 2000 MHz, with a frequency step of 6 MHz. The GPR system was mounted on a four-wheel motorcycle and combined with a laptop and a DGPS to allow for fast data acquisition.

3.2.3. Results and conclusion

Figure 19 shows the first layer dielectric permittivity (ε) from GPR inversion as a function of the measured volumetric water content (θ). The model of Ledieu et al. (1986) assuming a linear relationship between $\sqrt{\varepsilon}$ and θ was fitted on the observed data. The fit is very good, with a RMSE of 1.65 in terms of dielectric permittivity, denoting the high capability of the GPR inversion method to retrieve dielectric permittivities, given the inherent uncertainties in volumetric water content measurements due to the different support scales.

Although interferences phenomena, occurring with smallest layer thicknesses, are accounted for in the electromagnetic model, a lower sensitivity of the model to the dielectric permittivity is expected to be observed for configurations with the thinnest first layers. Indeed, dielectric permittivities retrieved for the largest layer thicknesses (i.e., h_1 = 4 and 8 cm) are in a better agreement with measured water content compared to the values retrieved for thinner layers. It is worth noting that the expected range resolution (one quarter the wavelength) is about 1.5 cm for a central frequency of 1700 MHz and for a dielectric permittivity of 9.

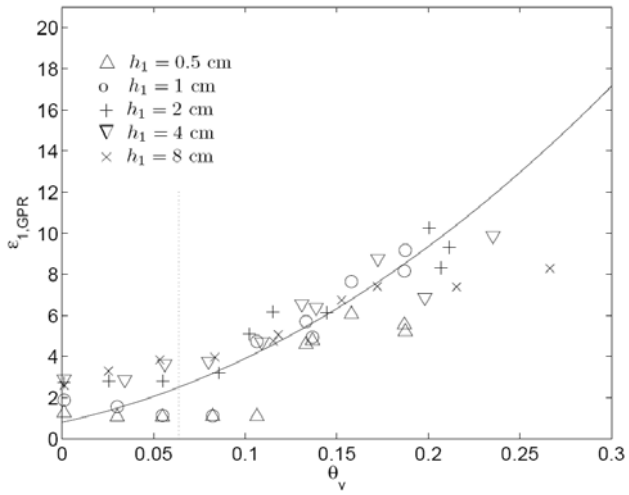

Figure 19: First layer dielectric permittivity estimated from GPR data inversion ($\varepsilon_{1;GPR}$) as a function of soil volumetric water content θ_v. Dielectric permittivities are depicted with different symbols according to the top layer thickness. The model of Ledieu et al. (1986) is fitted on the observed data (solid line).

Figure 20 (a) shows the surface soil water content map retrieved by one-layered model inversions of the 3741 points that were measured during the GPR field campaign. The mean volumetric soil water content is equal to 0.110 and its standard deviation is 0.0412. Soil water content patterns seem mainly explained by topography. A wet area can be observed in the North of the field, where a thalweg flows in the North-North-East direction. Hilltops are mainly dry, like in the South-East corner.

Two-layered inversions were also performed in a limited part of the field where layered conditions were in-situ observed (delineated with the red polygon in the one-layered map). First and second layer soil water content map are depicted in figure 20 (b) and (c). First layer soil moisture values are lower than the second layer values in a large majority of the points (91.3%), that is, at these locations, soil moisture increases with depth. First layer thicknesses are also optimized in the two-layered inversion and show values mainly between 3 and 5 cm.

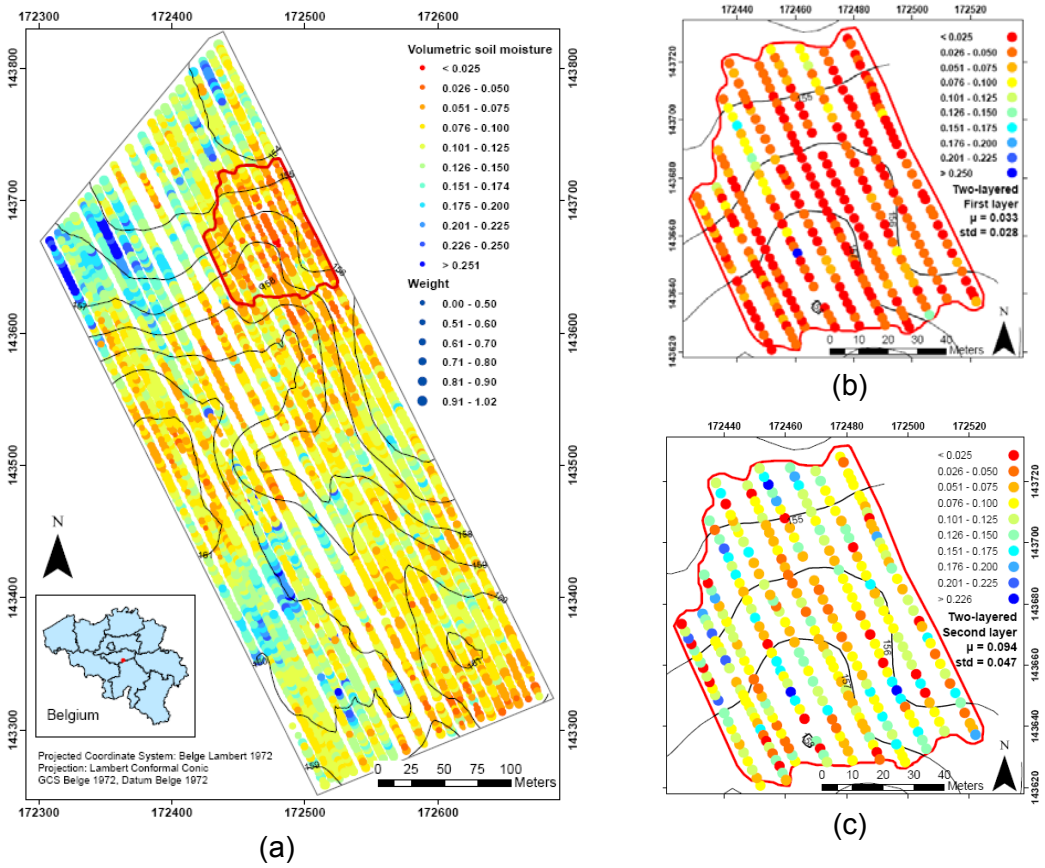

Figure 20: Surface soil water content mapretrieved by a) one-layered model and two-layered model: a) first layer c) second layer

3.2.4. Costs of the experiment and experimental difficulties

The GPR field campaign presented here lasted 3h30 for 3741 points mapped within a surface of 11 ha. Preparation of the GPR setup lasted less than 1 hour, so the mapping required only half a day on the field. Data processing for the one-layered soil moisture map need about an hour of computation time. Materials included a 4-wheel motorcycle, a laptop, the GPR system (VNA + cable + antenna) and a DGPS. Access to the field was allowed by the owner and transportation to the field necessitated the use of a car with a trailer.

The approximate cost of the materials involved is as follows: Quad 7k€, Field laptop 3 k€, VNA: 20 k€, Cable and calibration kit: 3 k€, Antenna: 5 k€, DGPS: 22 k€, resulting in a total of 60 k€. The number of person-day needed was 1.

4. Magnetism

4.1. INFLUENCE OF CARBON CONTENT AND CLAY CONTENT ON THE SOIL MAGNETIC PROPERTIES: A LABORATORY EXPERIMENT WITH THE SOIL FRENCH DATABASE

4.1.1. Objectives of the study

The aim of this study was to determine the influence of both carbon and clay content on the magnetic properties of soils (magnetic susceptibility and viscosity). In fact magnetic properties of soils are linked to their content in magnetic iron oxides and clay. In theory, the magnetic susceptibility is sensitive to both and the magnetic viscosity is only sensitive to magnetic iron oxides, as biogenic magnetic iron oxides have size near the limit between superparamagnetic and monodomain grain. The ratio of magnetic viscosity over magnetic susceptibility give then a qualitative information on the relative amount of magnetic viscous grain (possibly linked to organic matter) in the sample.

4.1.2. Materials and methods

The MS2D (Bartington Ltd) with the MS2D probe was used to measure the magnetic susceptibility. The TS6 (Protovale ltd) was used to measure the magnetic viscosity (these materials have been described in the D1.1 and D1.3). The measurements have been done on the soil French database samples (“Réseau de Mesure de la Qualité des Sols”) from the unit Infosol of the INRA center of Orléans. In order to evaluate the influence of the carbon and clay content, each sample has been chosen randomly with the constraint to be classified in class of clay and carbon content described in table 1. Consequently, one sample belongs to one class of carbon content and one class of clay content.

Clay content (g/kg)	0 - 50	50 - 100	100 - 150	150 - 200	200 - 250	250 - 300	300 - 350	350 - 400	400 - 450	450 - 500
Number of samples (clay content class)	10	10	8	7	9	7	9	6	8	5
Organic carbon content (g/kg)	0 - 2	2 - 4	4 - 6	6 - 8	8 - 10	10 - 12	12 - 14	14 - 16	16 - 18	18 - 20
Number of samples (carbon content class)	2	4	7	7	9	10	10	10	10	10

Table 1: Class of carbon and clay content used to choose the soil french database samples and the number of samples for each class

The figure 22 gives the position of the 79 samples randomly chosen in the soil french data base. The carbon content is the Y axis and the clay content is the X axis. The samples are stored in buckets, we choose to do the measurements without taking out the samples from there bucket, the devices loops were put on a wood table (figure 21).

Figure 21: a) the MS2B ready for measurements b) with a bucket sample

As the devices are calibrated for the response of a homogeneous halfground, the values measured on the buckets have to be corrected. The 3D response of the bucket was compute to define the multiplicative calibration factor. In fact, the apparent magnetic susceptibility is obtained with the measured value time a 1.47 factor and the magnetic viscosity is obtained with the measured value time a 1.55 factor.

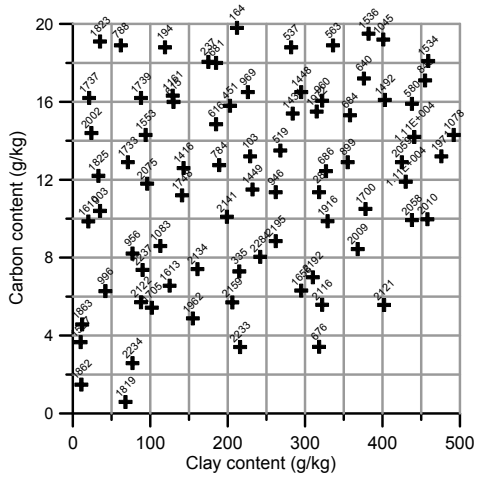

Figure 22: Position of samples in the carbon and clay content class

4.1.3. Results and conclusion

The results are shown in two steps, first the whole set of samples is presented versus clay and carbon content and finally, we focus on the samples under 250g/kg of clay.

Magnetic properties versus clay content

The results are shown in table 2. For clay content above 250g/kg, the magnetic variability seems to decrease (especially for the magnetic susceptibility data).This statement may suggest the fact that around 250 g/kg is a threshold value of clay content that changes the number of phenomenon influencing the magnetic properties. Under 250 g/kg, several processes competing; above, there are few processes dominating.

Clay content class (g/kg)	**Magnetic susceptibility (10^{-5} SI)** (mean / median / standard deviation)	**Magnetic viscosity (10^{-5} SI)** (mean / median / standard deviation)
0 - 50	7.3 / 4.4 / 6.2	0.050 / 0.021 / 0.056
50 - 100	26.2 / 20.2 / 17.3	0.148 / 0.054 / 0.190
100 - 150	44.9 / 38.2 / 32.8	0.320 / 0.366 / 0.201
150 - 200	32.9 / 19.1 / 42.8	0.144 / 0.110 / 0.175
200 - 250	44.2 / 23.5 / 52.6	0.272 / 0.138 / 0.278
250 - 300	22.8 / 27.2 / 9.8	0.206 / 0.214 / 0.162
300 - 350	23.9 / 26.5 / 16.4	0.150 / 0.126 / 0.181
350 - 400	21.9 / 18.4 / 14.5	0.223 / 0.185 / 0.195
400 - 450	20.9 / 18.4 / 14.4	0.144 / 0.100 / 0.182
450 - 500	15.6 / 12.5 / 9.4	0.071 / 0.044 / 0.055

Table 2: Mean, median and standard deviation on the magnetic properties measured for each carbon content class

Magnetic properties versus carbon content

Table 3 shows the values of respectively magnetic susceptibility and viscosity for each class of carbon content.

Carbon content class (g/kg)	**Magnetic susceptibility (10^{-5} SI)** (mean / median / standard deviation)	**Magnetic viscosity (10^{-5} SI)** (mean / median / standard deviation)
0 – 2	11.8 / 11.8 /12.5	0.034 / 0.034 / 0.033
2 – 4	24.3 / 14.7 / 21.7	0.176 / 0.071 / 0.266
4 – 6	22.5 / 11.8 / 29.5	0.123 / 0.039 / 0.204
6 – 8	35.5/ 14.0 / 43.3	0.188 / 0.096 / 0.219
8 – 10	23.2 / 9.6 / 35.4	0.173 / 0.058 / 0.261
10 – 12	26.7 / 21.3 / 17.3	0.177 / 0.140 / 0.152
12 – 14	19.7 / 17.6 / 12.3	0.153 / 0.124 / 0.128
14 – 16	30.1 / 16.2 / 42.8	0.197 / 0.080/ 0.242
16 – 18	25.6 / 30.1 / 11.9	0.195 / 0.167 / 0.155
18 - 20	30.7 / 22.8 / 25.5	0.191 / 0.126 / 0.182

Table 3: Mean, median and standard deviation on the magnetic properties measured for each carbon content class

The magnetic properties seem to slightly increase with the carbon content. In order to confirm these trends, a principal component analysis (PCA) has been performed with some other data taken in the French soil database. The results are presented on the figure 23 for the first and second component expressing 71% of the total variance for the whole set of samples (figure 23 a), 67% of total variance for the 0-250 clay content classes and 66%.for the 250-500 clay content class. Table 4 gives the correspondences between the letter displayed on the plots and the data used.

Data used in the PCA	Corresponding letter on plots
Clay content	A
Carbon content	B
Total nitrogen	C
Water pH	D
Cation exchange capacity	E
Magnetic susceptibility	F
Magnetic viscosity	G
Magnetic properties ratio	H

Table 4: Correspondences between the labels on the plots and the properties analyzed

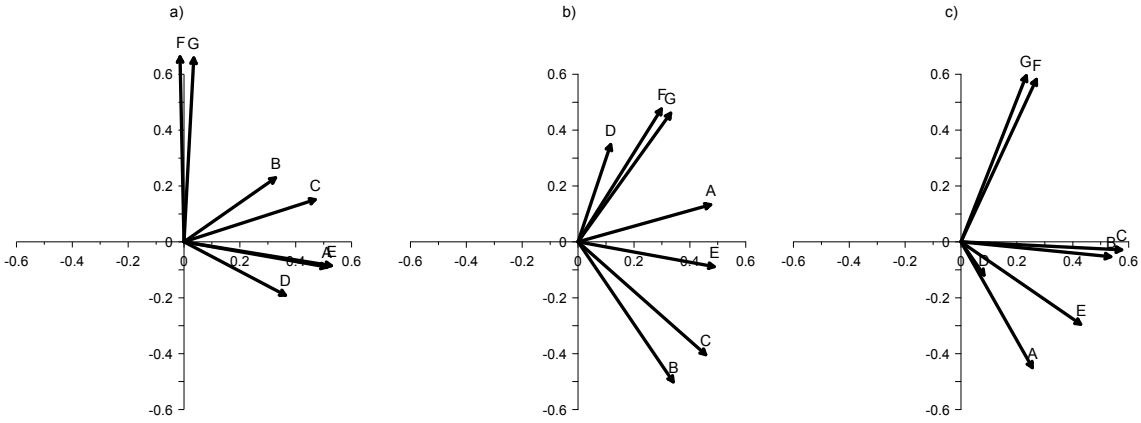

Figure 23: Principal component analysis results for a) the whole samples, b) sample with clay content between 0 and 250 g/kg c) samples ith clay content beetween 250-500 g/kg

What appears on figure 23 is the very strong correlation between the two magnetic properties (G and H). This could illustrate the fact that the response of the magnetic iron oxides dominates the paramagnetic one of the clay (A). For the whole set of samples (figure 23a), the magnetic properties appears to be mostly uncorrelated with the other parameters. This could indicate that the magnetic properties are relevant in a pedological approach. For the samples with clay content under 250 g/kg (figure 23b), it appears that:

- Magnetic properties (F and G) are correlated to pH (D) and slightly to clay content (A).

- Magnetic properties (F and G) are rather anticorrelated to carbon and nitrogen content (B and C).

Looking to the samples with clay content above 250g/kg (figure 23c), it appears that:

- Clay content (A) and pH(D) are collinear and rather anticorrelated to magnetic properties (F and G).

This could indicate that the clay content is the key parameter for the pH on these samples. The anticorrelation could indicate that higher clay content have less magnetic iron oxides.

As the two magnetic properties seem to bring the same information, we compute the PCA with the magnetic susceptibility and the magnetic properties ratio. The results are shown on figure 24.

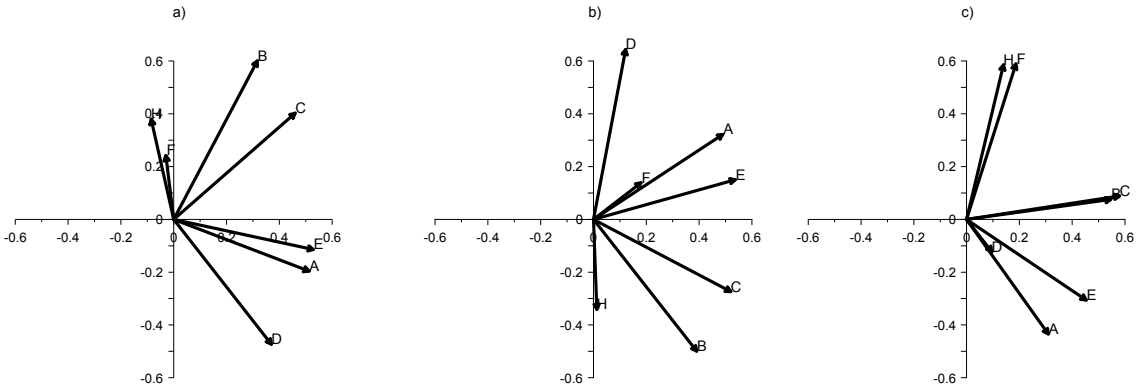

Figure 24: Principal component analysis results for a) the whole samples b) sample with clay content between 0 and 250 g/kg c) samples ith clay content beetween 250-500 g/kg

For this analysis, the two first principal components express 67% of the total variance for the whole set of samples (figure 24a), 64% of the total variance for the samples with a clay content between 0-250 g/kg (figure 24b) and 62% for the samples with clay content between 250 – 500 g/kg (figure 24c).

The PCA results differ from the first ones. For the whole sets of samples, magnetic susceptibility (F) and magnetic properties ratio (H) are rather correlated to carbon content (B) and well anticorrelated to pH (D)

Looking for the samples with clay content under 250 g/kg (figure 24b), it appears that:

- Clay content (A) and magnetic susceptibility (F) are correlated.

- Magnetic properties ratio (H) and pH (D) are anticorrelated.

- Magnetic properties ratio (H) and carbon content(B) are rather correlated.

  As the ratio express the relative amount of viscous ferromagnetic iron oxides grains, it seems that, for these samples, it is the clay content and/or superparamagnetic (or very viscous grain) which dominate the magnetic susceptibility. The anticorrelation with the magnetic properties ratio could be explained if the magnetic susceptibility varies while the magnetic viscosity is rather constant.

  Looking for the samples with content above 250g/kg (figure 24c), it appears that:

- Magnetic susceptibility (F) and magnetic properties ratio (H) are correlated and anticorrelated with clay content (A) and pH (D).

Correlation between magnetic properties ratio and magnetic susceptibility could be explain by the preferential creating or disappearing of the magnetic viscous grain. It should be noticed that CEC (E) is the only parameter which seems almost all the time mostly uncorrelated with the magnetic properties.

Conclusion

The carbon content and the magnetic properties, especially the magnetic properties ratio, seem to be correlated. As the CEC appears to be the parameter the most uncorrelated with the magnetic properties, it could be of interest to express the carbon content as a function of magnetic properties and the CEC, the last one being directly proportional to electrical conductivity. In theory it would be possible to express the carbon content as a function of magnetic properties and electrical conductivity. According to the PCA, this fact is more reliable for clay content under 250 g/kg. Another point is the fact that, under this limit of 250 g/kg, under the magnetic properties are much more variable than over this limit. It could be a possible limitation of the method in very clayed soils.

4.1.4. Cost of the experiment and experimental difficulties

The data were acquired with specific devices which can be rented. A team of two peoples have done the whole measurements in two half days. With the data processing, the cost of the study is evaluated at 0.5 man/month. The main difficulties are to do the measurements in a magnetically undisturbed environment.

5. Hyperspectral

5.1. PREDICTION AND MAPPING OF SOIL PROPERTEIS USING HYPERSPECTRAL SENSORS: LABORATORY AND FIELD DATA FROM THE MUGELLO TEST SITE

5.1.1. Objectives of the study

The objective was to retrieve and characterize some physical-chemical parameters (SOC, clay minerals, iron oxides and $CaCO_3$ contents) of the cultivated layer (0-30 cm depth) of soils (Vertisoil and Entisoil) in the Mugello test area, from both airborne hyperspectral and field spectrometry surveys in the 400-2500 nm spectral range. Statistical analysis is used to investigate the possibility to predict the selected properties using high-resolution reflectance spectra and to identify the spectral regions contributing to prediction.
Hyperspectral images acquired in September 2009 with SIM.GA sensor are being processed and analyzed with the aim of mapping the distribution of the mentioned parameters in the test area, pointing to establish a reliable procedure useful for regional scale soil monitoring.

5.1.2. Materials and methods

Different airborne campaigns were performed for testing sensors and the acquisition system on the DST-UNIFI ultralight aircraft, boarding the SIM.GA hyperspectral image sensor from Selex-Galileo. A joint DIGISOIL campaign was performed on September 2009 in the Mugello test site (Tuscany, Italy). An ASD FieldSpec Pro portable spectroradiometer was used during the airborne campaign for ground measurements for the characterization of atmospheric conditions (solar radiance and irradiance for atmospheric removal) and for reflectance measurements on reference targets. Soil samples also underwent traditional laboratory analyses for determination of natural SOC (UCL), clay minerals, iron oxides and $CaCO_3$ contents (UNIFI). ASD FieldSpec was also used to obtain reflectance spectra from dried, crushed and sieved samples under controlled laboratory conditions. Different chemometric techniques (including PLSR and multiple linear regression) are being used to examine relationship between clay content, iron oxides, calcium carbonate and organic carbon content and the reflectance spectra and to identify the wavelengths contributing to prediction of these soil properties, with acceptable R^2 values. A cooperation with

the Louvain University (UCL) team for the comparison of PLS methods based on different laboratory datasets is foreseen.
Semi-empirical (ELM) and physically-based models (FLAASH) are used for inversion of spectral calibrated data acquired during the airborne campaigns to ground reflectance. GPS/inertial data recorded from the aircraft, as well as ground control points and an accurate digital elevation model of the area is also required for the geocoding chain of SIM.GA data.

5.2.3 Field Campaign

5.2.3.1 Data collection and soil analysis

The test area is located about 30 km north of Firenze and it is extended for about 20 km^2 to the north of the Sieve stream, left tributary of the Arno river, being centred on the Figliano airport and comprised between the villages of Borgo San Lorenzo, Luco di Mugello and Scarperia.
The geological terrains outcropping in these zones are fluvio-lacustrine deposits, ranging in age between lower Pliocene and Upper Pleistocene, forming low-dipping lenticular beds. The landscape is typical of Tuscany intermontane basins, with gentle hills with low-altitude moderately dipping or level surfaces of alluvial origin as well as fairly- to highly-inclined downs. Climate is temperate-hot, with cold winters and mildly hot to hot summers and medium to intense rainfalls, concentrated in the autumnal months. From the pedological point of view, more or less eroded soils prevail (utric and calcareous Regosols and lytic Leptosols), soils with pedogenetic structure at depth and weakly differentiated profiles (eutric and calcareous Cambisols), soils with clay masses (gleich Luvisols), acidic soils with accumulation of organic material (humic Umbrisols) and anthropically terraced soils (anthropic Regosols). Agriculturally suitable terrains are assigned mainly to annual crops, marginally to olive groves, vineyards and orchards.

Ground sampling was carried out during the joint UNIFI-GAV-UCL-BRGM campaign on September 21st-24th 2009. About 80 topsoil (to a maximum depth of 5 cm) samples scattered all over the area were collected in order include as much spectral variability as possible in the calibration models. Samples positions were recorded with a differential GPS receiver.

5.2.3.2 Laboratory analyses

While analyses for SOC content were performed by UCL, UNIFI has in charge to carry out the analyses on clay minerals, iron oxides and calcium carbonate.

The samples collected in the field were crushed and sieved to obtain two granulometric classes:

- < 425 µm ,
- < 75 µm.

The laboratory spectral library was realized using a FieldSpec Pro spectroradiometer (Analytical Spectral Devices), measuring reflectance in 3-10 nm bandwidths over the range 350-2500 nm, provided with an illuminating device with stabilized krypton lamps, with fixed viewing and shooting geometry. Spectral reflectance measurements were repeated for both the granulometric classes, in order to improve the correlation with chemical/mineralogical data at a certain grain size.

Iron content was determined by the estimation of the amount of Fe^{3+} and Fe^{2+} in the samples, performed on the <425 µm fraction dried overnight at 105°. Iron was firstly extracted from soil with an acid attack using a 1M solution of HCl. Fe^{2+} was then determined through spectrophotometry, while Fe^{3+} was obtained as difference between total iron and Fe^{2+}.
For calcium carbonate, the CO_2 pressure developed during acid attack with a 1M solution of HCl was determined with a manometer (calcimeter method) and corrected for atmospheric pressure.

The quantitative determination of clay minerals contained in 40 of the 80 samples collected in the Mugello test site were conducted by Dr. Luca Lutterotti (Department of Material Engineering and Industrial Technologies). The procedure includes sample preparation through milling and sieving to obtain a ≤ 75 µm powder, which is subsequently compressed with an uniaxial cold-pressing method using a piston in a resin cylinder, which protects the sample. X-ray diffraction measurements in reflection or transmission were performed with a PANalytical X'Pert Pro powder diffractometer, provided with an image plate. This device allows to catch the diffracted radiation from a very wide 2θ angle (up to 100°), allowing to improve confidence in statistics, sensibility towards minor phases and possibility to correct for texture, thanks to the opportunity to collect a high intensity radiation, suitable for Rietveld quantitative analyses.

This procedure has especially been conceived for clay minerals, which generally show :

- preferential orientation;
- layer intermixing and turbostatic disorder;
- variability in interlayer water and cations.

The subsequent step is the qualitative analysis, which allows recognizing the phases, through search-match of the peaks. Then, images are processed with the Rietveld code MAUD (Lutterotti et al., 1997, 2007) using the single layer theory (Ufer et al., 2004, 2008) to take into account the turbostatic disorder.

Table 5 summarizes preliminary results:

Quartz	18-42%
Calcite	0-23%
Albite	0-19%
Illite	21-36%
Kaolinite	0-6%
Montmorillonite	0-35%

Table 5: Mineral compôsition of Mugello soil samples

5.2.3.3 Statistical analysis and prediction of soil properties

Chemical/mineralogical records are tentatively being correlated with reflectance data in order to obtain relations or statistical models based on the following procedures:

Soil Parameters	Methods
Iron Oxides	Band-Depth correlation (peak at 550 nm) after convex-hull removal and spectra normalization
Total Clay Minerals	Band Depth at 2210 nm after convex-hull removal and spectra normalization; alternatively partial least square regression (PLSR)
Single Clay Minerals	Spectra Unmixing by means of VCA (Vertex Component Analysis); alternatively PLSR or multiple linear regression (MLR)
Calcium Carbonate	Band-Depth correlation (peak depth measured 2348 nm), after continuum removal and normalization of spectra; alternatively PLSR
Organic Carbon	PLSR

Table 6: Statistical approaches proposed for each soil chemical/mineralogic parameter

VCA (and Bioucas Dias, 2005) is a linear unmixing method, which allows to estimate the number of reference substances (endmembers) starting from a set of Vertex Component Analysis) algorithm (Nascimento mixed spectral (multispectral or hyperspectral) vectors, yielding their spectral signatures and their abundance fractions. On Mugello dataset, VCA analysis revealed the presence of only two distinguishable endmembers, corresponding to illite and montmorillonite (figure 25). There is no significant correlation between unmixing percentages and the composition resulting from mineralogical analyses.

Figure 25: Clay endmembers resulting from VCA

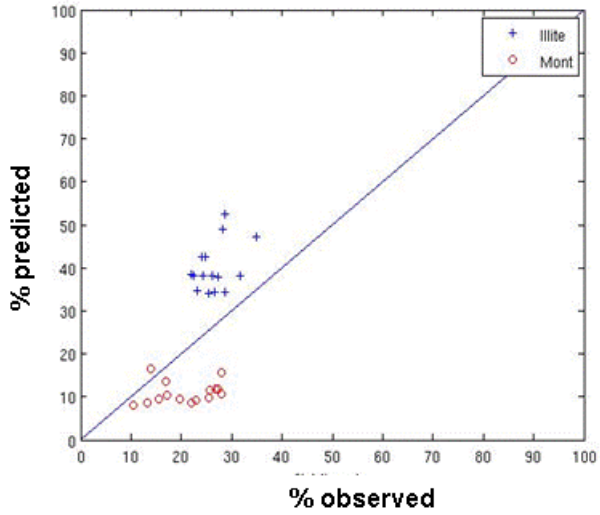

Figure 26: Predicted vs observed values for MLR applied to clay mineral content in Mugello soil samples

MLR is a common multivariate tool which specifies the relationship between a response variable (Y) and a set of dependent variables (X), managing nonlinearity by adding new terms to a polynomial function (eq. 2). Significant limitations, such as the overfitting of data, often affect this method applied to hyperspectral reflectance measurements. The hypothesis of using this approach for statistical treatment of clay minerals data implies least square regression and is based on the assumption that absorption peaks at 1414 nm, 1919 nm and at 2210 nm in soil sample spectra are determined by the linear superposition of the contributes of a little number of minerals, according to the following:

$$P=\Sigma a_i x_i+b \qquad \text{(eq. 2)},$$

where P is absorption peak depth, x is concentration of a certain mineral and b is a correction factor for inferring absorbance; assumption of linearity has to be demonstrated and it is generally problematic when handling illite.
The Mugello dataset was split into two parts: 25 calibration samples for calculating a_i coefficients and 15 samples for method's validation. This method was preliminarily tested with a laboratory dataset obtained from mixtures of illite, kaolinite and montmorillonite at several concentrations, with resulting R^2 values for the calculation of a_i comprised between 0.90 and 0.98. The same algorithm was then applied on natural samples, hypothesizing a two-component mixture (since kaolinite percentage is negligible), yielding R^2 values of 0.68 and 0.69 (determined at 1414 nm and 1919 nm respectively). Once coefficients have been calculated, the same polynomial function is used to obtain concentrations. As showed in figure 26, an overestimation of the real concentration of illite and a correspondent underestimation of montmorillonite content affects present application of this method.

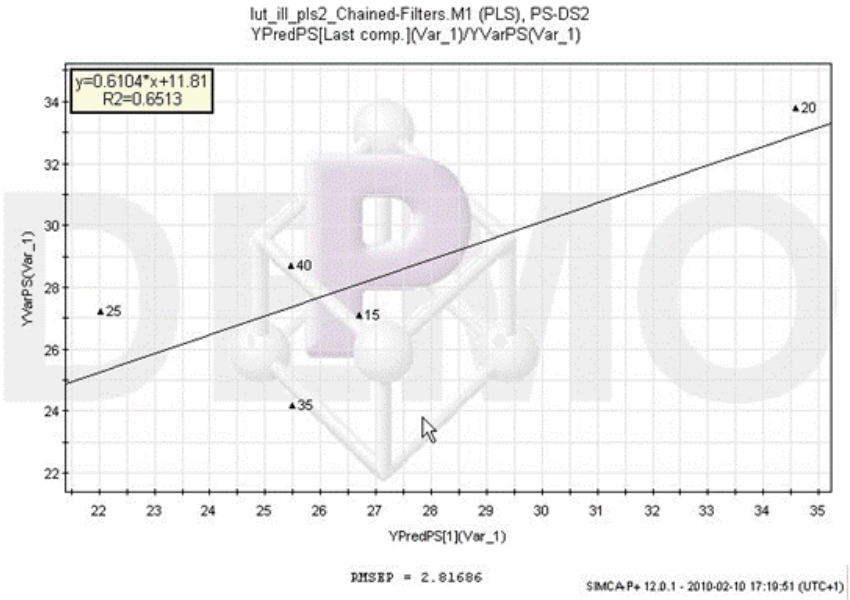

Figure 27: one composent SIMCA model on illite content in Mugello soils

In the **PLSR** approach (Wold et al., 1983, 2001; Otto and Wegscheiderm 1985), predictors (X variables) and responses (Y variable) are projected into a low-dimensional space (i.e. a set of orthogonal variables called Latent Variables), maximizing the co-variance between X- and Y-scores. PLSR was carried out using both The Unscrambled (Camo Software AS) and SIMCA P+ (Umetrics) software tools, as to have a proof of the method's robustness. Pre-processing using Standard Normal Value (SNV)+Orthogonal Signal Correction (OSC) filters and removal of 3 outliers were applied. Three fourths of the dataset were used in the calibration set and the rest for validation purposes. A one component SIMCA model yielded the following results (figure 27):

$$R^2X = 0,44; R^2Y = 0,98; Q^2 = 0,97$$

As showed in figure 28, by plotting absorption peak depth at 2210 vs clay mineral total content, a R^2=0.6 is obtained (band-depth analysis), while PLRS yielded a R^2 value of 0.48.

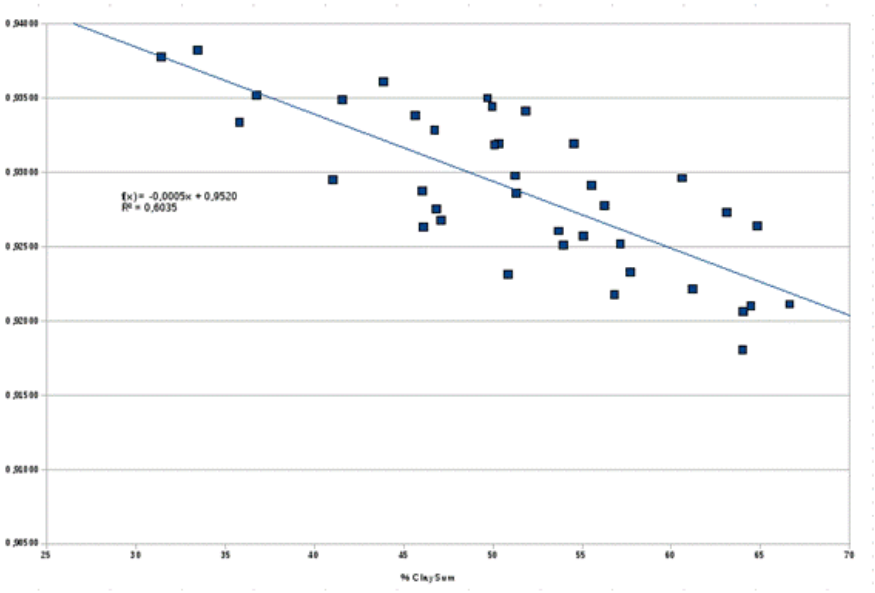

Figure 28: Results of band depth analysis on total clay content in Mugello soils

5.2.4 Airborne Campaign

5.2.4.1 Data acquisition

Two preliminary flight campaigns allowed installation of SIM.GA on board of UNIFI ultralight aircraft as well as flight software updating (23/4/2009) and boresight geometric calibration of SIM.GA (07/05/2009). DIGISOIL flight campaign for acquisition of hyperspectral images was carried out by the GAV-UNIFI team, in cooperation with UCL and BRGM, in the Mugello test site (WGS84 coordinates approximately: Lat.=43°58.6 N, Long.=11°21.9 E), on September 21st-24th 2009. This period was selected for flight and ground data collection, according to the typical climate in Italy, in order to ensure cloudless sky, high sun illumination conditions and large availability of bare soils, with a minor amount of cultivated ones (vineyards, corn, alfalfa). A pilot survey allowed establishing a flight plan including five flight paths about 350 m wide and about 3-5 Km long (figure 29). The approximate pixel resolution was 0.6 m (VNIR) and 1.2 m (SWIR) considering a height of flight of about 900 m.
A dedicated photogrammetric aerial survey was performed and the resulting digital elevation (0.5 m 3D precision) model is under elaboration.

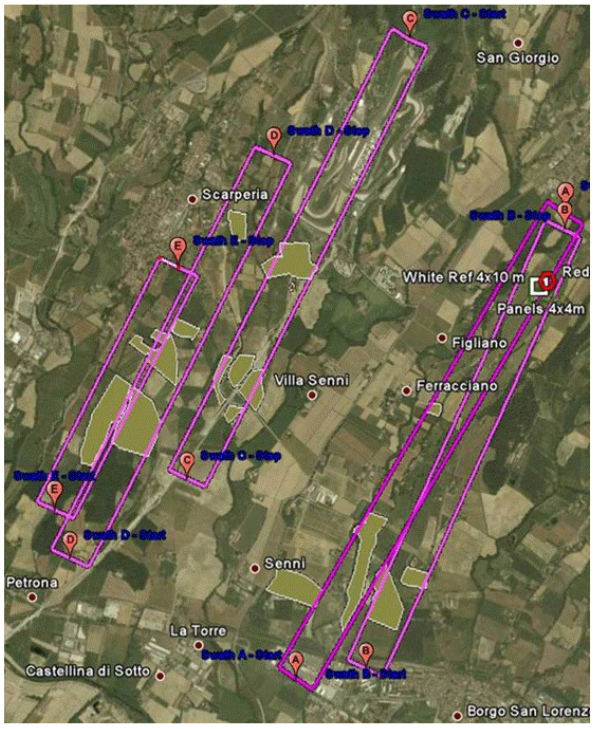

Figure 29: Flight plan for DIGIDOIL September 2009 campaign

5.2.4.2 Data elaboration techniques

Collected raw data (L0a) include separate VNIR and SWIR raw DN data blocks in ENVI format and navigation INS/GPS data. As shown in the workflow of figure 30, SIM.GA row data were firstly transformed into at-sensor radiance values (L1a), where calibration coefficients and parameters from laboratory measurements are applied to non-georeferenced VNIR/SWIR DN values.
Then, geocoded products are retrieved for each flight line by using a procedure developed in IDL Language and PARGE (PARametric Geocoding) software.

The PARGE outputs for each HYPER image are:

- *igm file (Lat/Long Geographic LUT for ENVI)
- *sca file (scan zenith/azimuth angles and altitude for ENVI).

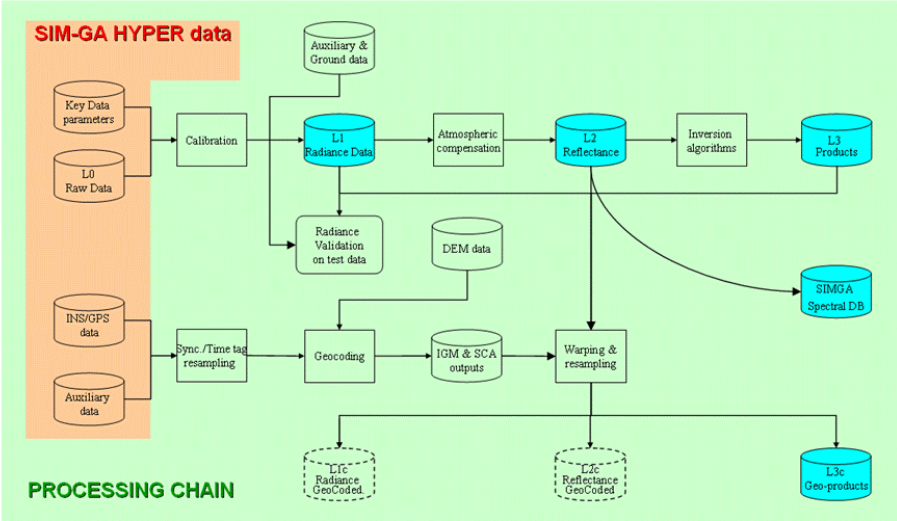

Figure 30: Hyper SIM.GA data processing chain

When all compensation parameters are applied to HYPER data or to the final thematic map (e.g. SOC, CLAY, etc) ortho-rectified, geo-referenced and co-registered VNIR to SWIR images or maps are produced and available for GIS application and 3D view as shown in figure 31 and 32.

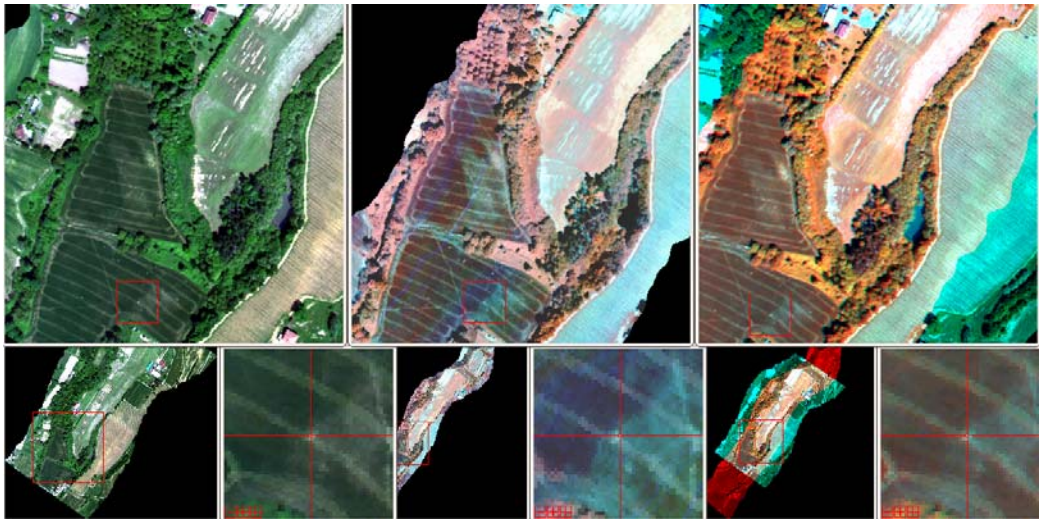

Figure 31: Coregistration of VNIR and SWIR channels after application of boresight offsets

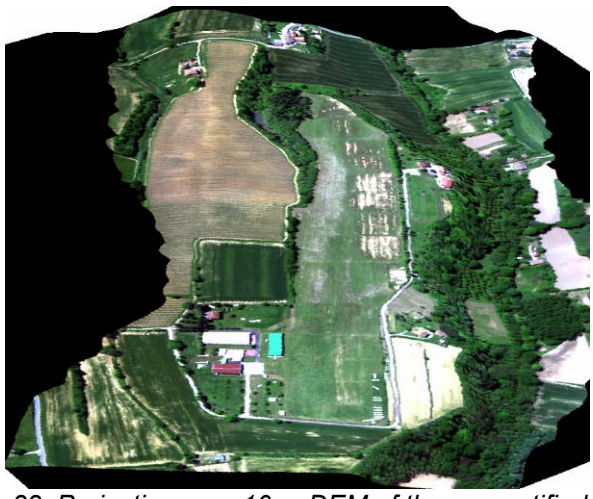

Figure 32: Projection over 10 m DEM of the georectified image

According to the physically-based approach, airborne imagery have to be corrected for the influence of the atmosphere, solar illumination, sensor viewing geometry and terrain geometry information, for the retrieval of inherent surface reflectance properties. Surface reflectance is commonly considered the basic product (L2) which is function, through complex relationships, of different geophysical parameters that have to be investigated and retrieved by means of inversion algorithms (L3).
Calibrated radiance data were inverted into geometrically and atmospherically corrected at-surface reflectance values, using semi-empirical (ELM) and physically-based models (FLAASH). **FLAASH** (Fast Line-of-sigh Atmospheric Analysis of Spectral Hypercubes) considers only the medium value of altitude in the image and adopts MODTRAN (MODerate resolution TRANsmitance code) codes as a model to simulate the calculation of radiative transfer, using flight data as input parameters, allowing to model atmospheric configuration. **ELM** (Kruse et al., 1985), instead, requests reflectance measurements at ground collected during flight, in order to convert radiance into reflectance and assumes atmosphere as being uniform, establishing a linear correlation between radiance and reflectance for every band of the image.

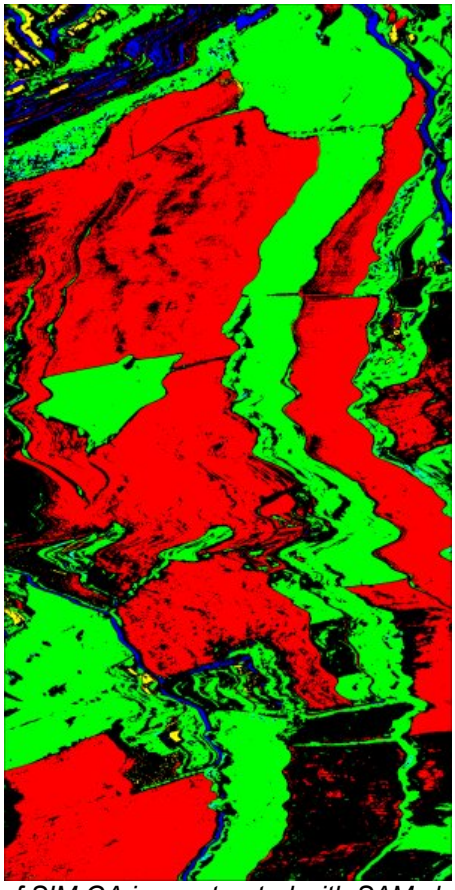

Figure 33: Example of SIM GA image treated with SAM classifier; R=bare soils; G=vegetation; Y=roofs; B=roads

Once the reflectance image is obtained, it undergoes spectral classification through dedicated algorithms; every pixel of the image is classified on the basis of spectral resemblance, depending on the occurrence of a certain material and possibly on its relative abundance. The collected images were elaborated using ENVI software (ITT VIS, Boulder, CO). Present attempts gave results as shown in figure 33, obtained by applying smoothing and supervised SAM classifier (Kruse et al., 1993), which uses the n-dimensional angle to compare image spectra to the reference spectra (training area) in the image, treating the spectra as vectors in a space with dimensionality equal to the number of bands. The algorithm then compares the angle between the reference spectrum vector and each pixel vector in a n-dimensional space. Smaller vector angles between spectra represent closer matches to the training area spectrum and can be grouped into the cluster represented by the reference spectrum.

5.2.5 Results and conclusion

Kriged geographic distributions of the measured parameters are being overlaid on topographic and geo/pedologic maps, in order to analyze the relationships

between chemical/mineralogical features and geology/geomorphology. These preliminary results shall be tuned and object of spectroscopic investigation during the project. Soil composition, generally homogeneous because of the uniform geo-pedological characteristics of the test site, could show subtle relationships with mineralogical data for different slope positions corresponding to the occurrence of either soil, eroded soil or colluvium
Uncertainties in clay content predictive models lead to the necessity of attempting new statistical approaches and to develop new dedicated algorithms. Granulometric determinations will be performed in the effort to shed light on some mineralogical anomalies and to establish a correlation between grain size and spectral response.
The 2210 nm peak seems to be the only distinctive one for the detection of clay minerals by means of hyperspectral remote sensing. Thus, preliminary results point to the possibility to use upscaling of laboratory mineralogical data to map total clay content in soils from remotely sensed images. Feasibility of prediction through statistical analysis will be tested for further laboratory responses on the concentration of $CaCO_3$ and iron oxides.

5.2.6 Costs of the experiment and experimental difficulties

The total cost of this experiment was 6 person-month. The prediction of soil clay content is affected by uncertainties in the statistical analysis due to the difficulties encountered in performing an effective unmixing, since all clay minerals share the main absorption peaks, so that none of them is diagnostic. Thus, the classical correlation between concentration and band depth cannot be achieved.

Some of the encountered experimental difficulties are linked to the necessity to improve SIM.GA workability on board of the UML, with enhancements on software and hardware, as for instance:

1. improvement of acquisition software
   - changes to graphics interface
   - simplification in flight software for user
   - automation of software initialization
   - development of error messages and data logging
   - increased possibility of saving ancillary data;

2. development of a C++ acquisition software for synchronization of GPS-INS data;

3. adjustment and testing optical heads power supply system, in terms of autonomy, weight and encumbrance (table 7 and figure 34);

4. HW definition, assemblage and testing of new server.

Weight	Power	Autonomy	Storage	Overall Size
80	550	1	200	85x37x70
60	370	1.5	600	85x37x55 (battery included)
-20 Kg	-180 W	+0.5 h	+400 GB	-15 cm (H)

Table 7: HD and SW improvements performed on SIM.GA on board of UNIFI ULM

Figure 34: Development of SIM.GA-ULM improvements from first integration to the present one.

5.2. SOIL ROUGHNESS AND BIDIRECTIONAL REFLECANCE: A LABORATORY BRFD EXPERIMENT

5.2.1. Objectives of the study

The ability of imaging spectroscopy to cover large surfaces in a single campaign and study the spatial distribution of soil properties with a high spatial resolution represent a major opportunity for soil monitoring and the spatial predictions of soil properties. However, there are still major constraints to the widespread use of imaging spectroscopy for soil applications (Ben-Dor et al., 2009): (i) atmospheric absorptions, (ii) low signal-to-noise ratio and (iii) spatial variation in surface properties (e.g. soil roughness, crusting, vegetation residue, moisture). We will address here point (iii) mentioned above and, in particular, the impact of

roughness on soil reflectance. Soil roughness is indeed known to induce a significant anisotropy on the directional distribution of the solar radiation scattered from bare soils. This directional anisotropy generates variability in the across-track signal measured by a remote sensor since each pixel is measured from a different observation angle. An example of such effect as observed in a hyperspectral image taken on October the 6th 2007 by the AHS-160 sensor in the Grand-Duchy of Luxembourg is displayed in figure 35.

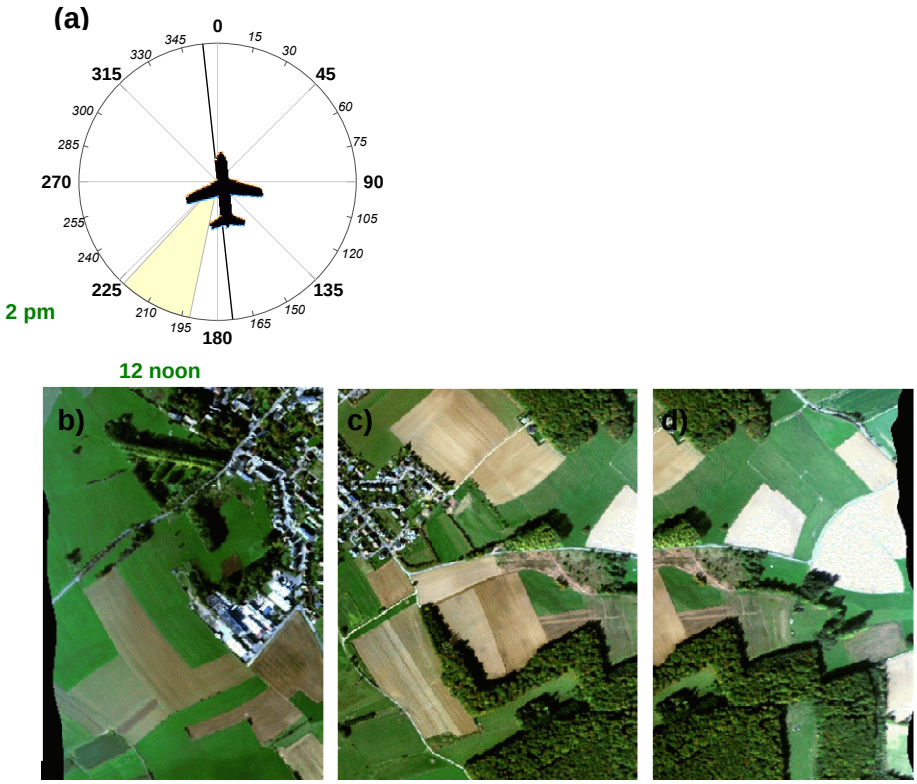

Figure 35: (a) Polar plot indicating the heading of a flight (black line) compared to the solar azimuth (yellow cone); (b)-(d) West-East transect of a colour composite hyperspectral image showing evidences of backscattering

For the time being, these variations, known as BRDF (Bidirectional Reflectance Distribution Function) effects, are poorly taken into account in the prediction of soil properties. It has been shown elsewhere that empirical/statistical approaches to retrieve soil properties from Hyperspectral Remote Sensing (HRS) data are very sensitive to small difference in the predictors due to variation in measuring conditions (Stevens et al., 2008). Soil roughness may therefore decrease dramatically the accuracy of such approaches, particularly when using sensors having large Field of View (FOV). In the following, we describe a laboratory experiment aiming to study the BRDF of a soil with different roughness characteristics. We will exploit in the future the output of this research to improve

quantitative predictions of soil organic carbon prediction by correcting available HRS data using the method proposed in Feingersh et al. (2010).

5.2.2. Materials and methods

Estimating BRDF

Let us first note that the *reflectance* (ρ) is defined as the ratio of the radiant exitance (M [W m^{-2}]) with the irradiance (E [W m^{-2}] and the *reflectance factor* (R) as the ratio of the radiant flux reflected by a surface to that reflected into the same reflected-beam geometry and wavelength range by an ideal and diffuse standard surface, irradiated under the same conditions (Schaepman-Strub et al., 2006). The Bidirectional Reflectance Distribution Function (BRDF) describes the scattering of a parallel beam of incident light from one direction in the hemisphere into another direction. Following the definition of Nicodemus et al. (1977), BRDF is the ratio of the reflected radiance L_r [Wm^{-2} sr^{-1} nm^{-1}] in one specific direction θ_r, Φ_r (θ and Φ represent respectively elevation and azimuth angles; subscript *r* stands for "reflected") and the incident irradiance E_i [Wm^{-2} nm^{-1}] from another direction θ_i, Φ_i (subscript *i* stands for "incident"; eq.3).

$$BRDF(\theta_i;\phi_i;\theta_r;\phi_r,\lambda) = \frac{dL_r(\theta_i;\phi_i;\theta_r;\phi_r,\lambda)}{dE_i(\theta_i;\phi_i,\lambda)} \quad [sr^{-1}] \qquad \text{(eq.3)}$$

Since it is a ratio of infinitesimal quantities, BRDF cannot be measured. Other relevant conceptual or measurable quantities can be derived by integration of eq.3 over corresponding finite solid angles (see Schaepman-Strub et al., 2006). When measuring the reflectance properties of a surface, we follow the concept of reflectance factor and use the Bidirectional Reflectance Factor (BRF) rather than the BRDF. BRF is the ratio of the reflected radiant flux from the surface area d*A* to the reflected radiant flux from an ideal and diffuse surface (e.g. a Spectralon© plate) of the same area d*A* under identical view geometry and single direction illumination (Schaepman-Strub et al., 2006; eq.4)

$$BRF(\theta_i;\phi_i;\theta_r;\phi_r;\lambda) = \frac{d\mathbf{L}_r(\theta_i;\phi_i;\theta_r;\phi_r;\lambda)}{d\mathbf{L}_r^{id}(\theta_i;\phi_i;\lambda)} \quad \text{[dimensionless]} \qquad \text{(eq.4)}$$

where superscript *id* stands for "ideal (lossless) and diffuse (isotropic or Lambertian)". The BRF, being bidirectional, is also a theoretical quantity that cannot be measured. As a matter of fact, in the laboratory, measurements generally consist of Bi-Conical Reflectance Factor (BCRF) since both illumination and observation geometries are conical (Schöpfler, 2008). However, the conicality is often neglected and the resulting measurements are often loosely

called BRF. Another approximation to the BRF is introduced by measuring only at selected positions over the hemisphere. The whole hemisphere is then estimated by interpolating values between sampled sensor positions (Feingersh et al., 2010). The BRF can be further normalized to a reference spectrum in order to enhance anisotropy patterns (Sandmeier et al., 1998). The reference spectrum can be either the BRF at the nadir position (θ_r=90°) or the mean BRF over the hemisphere (corresponding to the Bi-Hemispherical Reflectance or BHR if diffuse irradiance is neglected). The outcome of this operation is called the Anisotropy Factor (ANIF) and is given by eq.5.

$$\begin{cases} ANIF(\theta_i;\phi_i;\theta_r;\phi_r;\lambda) = \dfrac{BRF(\theta_i;\phi_i;\theta_r;\phi_r;\lambda)}{BRF(\theta_i;\phi_i;\theta_{nadir};\phi_r;\lambda)} \\ ANIF(\theta_i;\phi_i;\theta_r;\phi_r;\lambda) = \dfrac{BRF(\theta_i;\phi_i;\theta_r;\phi_r;\lambda)}{BHR(\theta_i;\phi_i;\lambda)} \end{cases} \quad \text{[dimensionless]} \qquad \text{(eq.5)}$$

It should be noted that ANIF values usually do not exceed the range 0.5-5 at all wavelengths in the spectral range (Feingersh et al., 2009).

Goniometric measurements

Measurements of the BRF were realized at the Israeli Goniometric Facility (IGF), established in the Remote Sensing Laboratory of Tel Aviv University (Feingersh et al., 2005). This equipment allows a mounted spectrometer to make measurements from any angular position θ_r, Φ_r in a hemisphere (figure 36). The illumination source, which is also attached to the goniometer, can be rotated as well. Spectral measurements were taken with an FieldSpec Pro FR spectroradiometer (ASDinc., Boulder, USA), characterized by a Full Width Half Maximum of 3 nm for the 350-1000 nm region and 10 nm for the 1000-2500 nm region. The spectrometer was positioned at a distance of 60 cm from the target with a 8° fore-optic, resulting in a ground IFOV of 8.4 cm at nadir position. The illumination source was placed at a distance of 60 cm from the target and consisted in two Lowel Pro-light with 14.5V Bulb/128690 tungsten halogen bulb and a beam width of 25°.

Figure 36: The Israeli Goniometric Facility (IGF) located at RSL-TAU (May 2009)

Radiance (L_r) measurements consisting of 40 samples per data value were taken at 97 positions in the hemisphere with θ_r in the interval [20°,90°] and resolution of 10° and with Φ_r covering 360° and resolution of 22.5° when θ_r < 70° and 45° when $\theta_r \geq 70°$. Three replicates of each position were recorded. During the measuring process, a dark current was collected at each change of θ_r using a white reference plate (Spectralon©) to optimize the spectrometer for illumination condition. This full set of goniometric measures was repeated for different illumination angular positions, with θ_i = [25°,35°,45°,55°,90°] and Φ_i = [0°,90°]. In order to obtain the BRF (see eq.4), the radiance of the white reference plate (L_r^{id}) was measured for each individual combination of θ_r, Φ_r, θ_i. The BRF was further interpolated to a finer grid using the *interp* function of the akima package in R (AKIMA, 2009; R Development Core Team, 2009).

Soil sampling and roughness

In order to conduct BRF measurements, approximately 100 kg of soil was collected in the plough layer of a cropland in the Oesling area (Grand Duchy of Luxembourg). The Oesling region is part of the Ardennes massif and lies on a substrate of Devonian slate with predominantly shallow sandy and sandy-loam soils (Dystric Regosols and Dystric Cambisols). A sub-sample (100 g) was sieved (2mm) and analyzed for Organic Carbon (OC) by dry-combustion with a LECO CN analyzer. The measured OC value is 1.94 g C kg^{-1}. The soil sample was air-dried and placed on a horizontal plate inside a graduated wooden frame of 1mx1m and 10 cm height (figure 36).

It was not feasible to reproduce in the laboratory exact roughness conditions as encountered in the field. Instead, three roughness conditions were arbitrarily created which are considered to represent three possible roughness classes observed in field conditions (figure 37a-c). The first roughness class (R1) was a horizontal surface with a small amount of aggregates (size ≤ 5 cm) and was thought to represent a field in seedbed condition (figure 37a). The second surface

(R2), being also horizontal, was much rougher than R1 since it was entirely covered by soil aggregates of varying size (≤ 8cm) (figure 37b). The third roughness class (R3) was a ridge-and-furrow surface with a ridge height of approx. 7-8 cm (figure 37c).

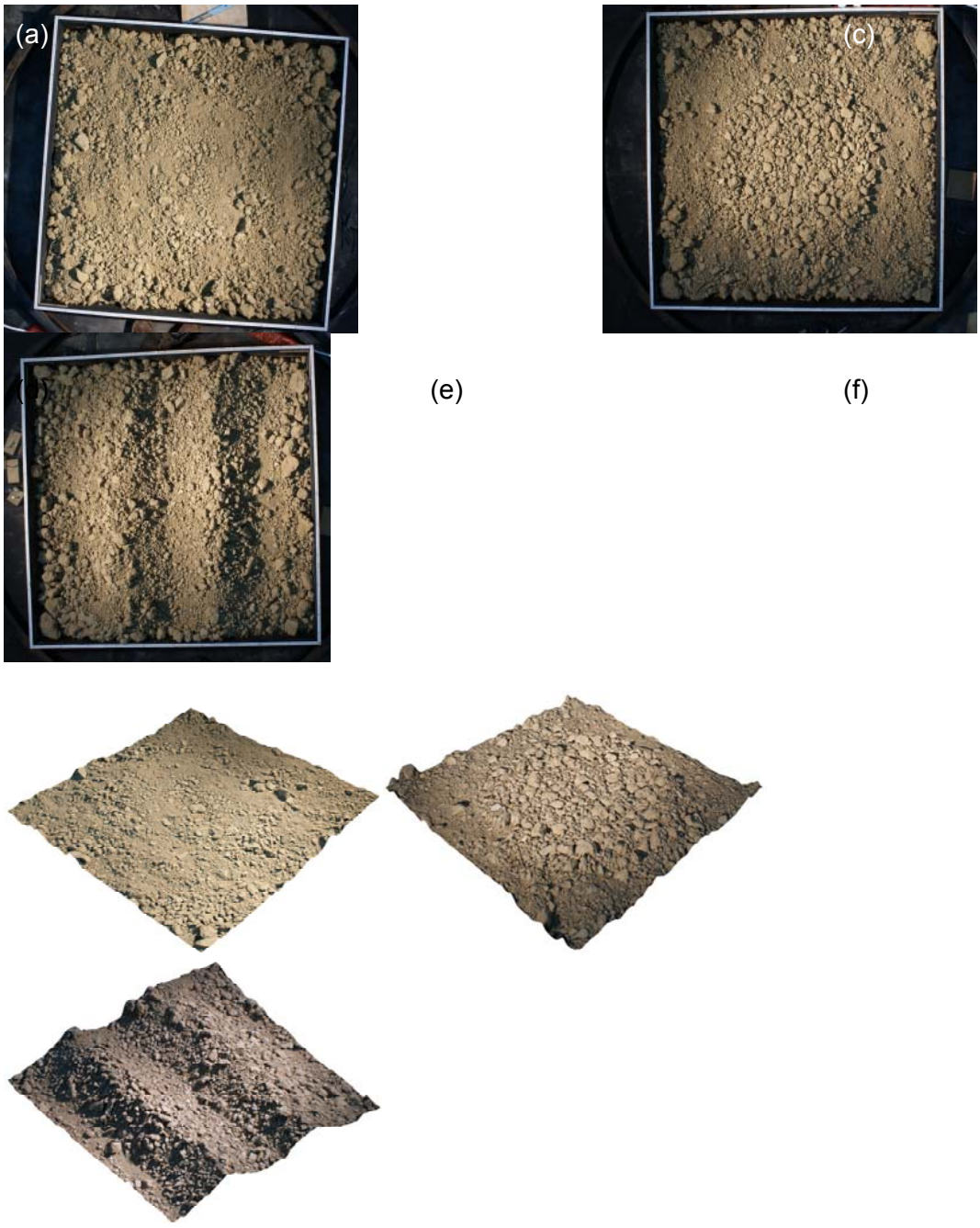

Figure 37: Digital photography of surface (a) R1, (b) R2 (c) R3; (d-f) 3D view of Digital Surface Models (DSM) as inferred from close-range stereoscopic measurements

In order to characterize these surfaces in terms of measurable quantities, Digital Surface Models (DSMs) were produced using stereo photogrammetric principles. Close range stereo photogrammetry can be a useful and quick tool to estimate soil roughness indices in the field or the laboratory (Zribi et al., 2000; Taconet and Ciarletti, 2007). However, the technique tends to produce smoother surface than laser scanning and may be inaccurate in shadowed zones or in fine structured areas with small aggregates and gaps (Jester and Klik, 2005). A pair of stereoscopic photos was taken for each roughness class with a digital Sony Alpha DSLR-A200 camera (10 Mpixels) and a focal length of 18 mm. The camera was attached to a horizontal metal bar with the CCD positioned at a height of 149 cm from the graduated wooden frame. Camera horizontality was continually checked with a spirit level during the time of the shot (1/8"). The pairs of images were processed with the Leica Photogrammetry Software (LPS9.3, Erdas, Atlanta, USA) and its Automatic Terrain Extraction (ATE) module. About twenty Ground Control Points (GCPs) were collected on the graduated wooden frame and a set of tie points were selected on both images. An automatic tie point collection was further run to increase the number of control points. Block triangulation was realized through the LPS self-calibrating bundle adjustment and finally the DSM was extracted (figure 37d-f). Due to lens distortion (camera is not calibrated), it was found that DSMs was inaccurate at the edges of the images. Thirty cm of the edges of each DSM were therefore cropped to keep only reliable data. The standard deviation (SD) of heights in the (x,y) directions were used to estimate roughness. Figure 39a shows that R1 is characterized by the lowest SDs in both x and y directions. R2 presents higher SDs than R1 but not as much as expected, probably due to the poor ability of the stereo photogrammetric technique in the modeling of shadowed area and small gaps between aggregates. While R1 and R2 show both equivalent estimates of SD_x and SD_y, R3 is characterized by very different SDs in the x and y directions due to the presence of oriented roughness.

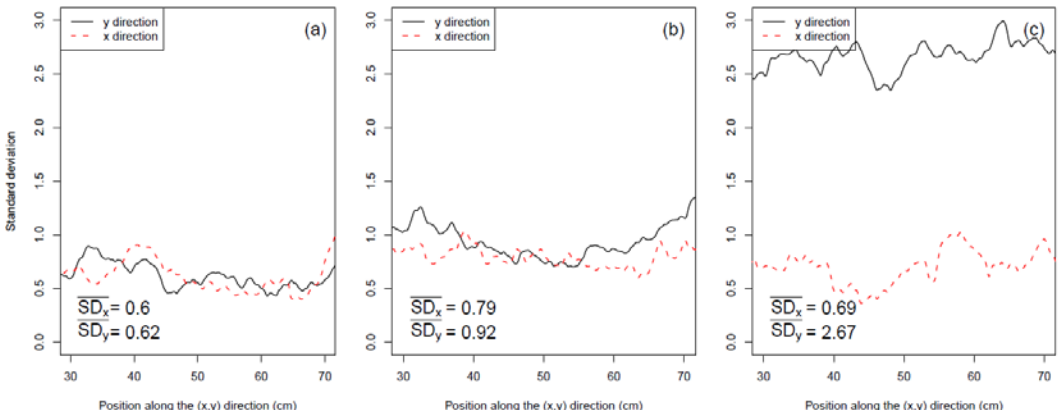

Figure 38: Standard deviation of DSM height in the (x,y) directions in (a) R1, (b) R2 and (c) R3 samples

In addition to roughness parameters, DSMs allowed us to compute the soil surface shadowing due to roughness. This is of critical importance because part of BRDF-related effects can be explained by the change in the proportion of

illuminated *vs* shadowed areas as a function of illumination and viewing geometry (Cierniewski and Courault, 1993). The computation of proportion of viewed shadow followed three steps. First, a low-pass filter was applied to the DSMs using ArcGis 9.3 (ESRI, Redland, USA) to reduce the significance of potential anomalous cells. Secondly, shadowed areas were computed using SAGA GIS (SAGA Development Team, 2008) and its Analytical Hillshading module with the Ray Tracing method. This procedure was repeated for each combination of illumination angles (θ_i, Φ_i) using the RSAGA package in R (Brenning, 2010; R Development Core Team, 2009). Finally, the proportion of sensor viewed shadow was computed with eq.6 for every possible sensor/illumination positions (θ_r, Φ_r; θ_i, Φ_i) using ArcGis geoprocessing scripts and Python 2.5 (Python Software Foundation, Hampton, USA).

$$SHADOW = 100 \times \frac{\sum (V(\theta_r, \phi_r) \times S(\theta_i, \phi_i) \times IFOV(\theta_r, \phi_r))}{\sum IFOV(\theta_r, \phi_r)} \quad \text{(eq. 6)}$$

with V, a binary (0,1) viewshed raster showing areas that are visible from a specific viewing location, S, a binary (0,1) shadow raster, IFOV, a binary (0,1) raster delimiting the ground IFOV of the sensor. The ground IFOV of the spectrometer was represented as the projection of an oblique cone (with FOV = 8°) on a horizontal surface, i.e. an ellipse with major axis and minor axis as given in eq. 7a-b.

$$2a = d \times \frac{\sin(2\alpha) \times \sin(\theta_r)}{\sin(\theta_r + \alpha) \times \sin(\theta_r - \alpha)} \quad \text{(eq. 7a)}$$

$$2b = d \times \frac{\sin(2\alpha) \times \sin^2(\theta_r)}{\sin(\theta_r + \alpha) \times \sin(\theta_r - \alpha)} \quad \text{(eq. 7b)}$$

with a = semi-major axis, b= semi-minor axis, d = distance to the target (cm), α = ½ FOV. The output of such computations can be integrated in a plot showing the variation of viewed shadow as a function of θ_r and Φ_r. An example is given in figure 39 for (θ_i, Φ_i) = (25°, 0°) showing, as expected, that R2 is the surface casting the most shadow on itself (figure 39b; up to 80-90% of shadow at such low illumination elevation angle). R1 and R3 surfaces are less affected by this phenomenon with a clear deviation of the circular pattern for R3 due to the presence of the ridges (figure 39a and 39b).

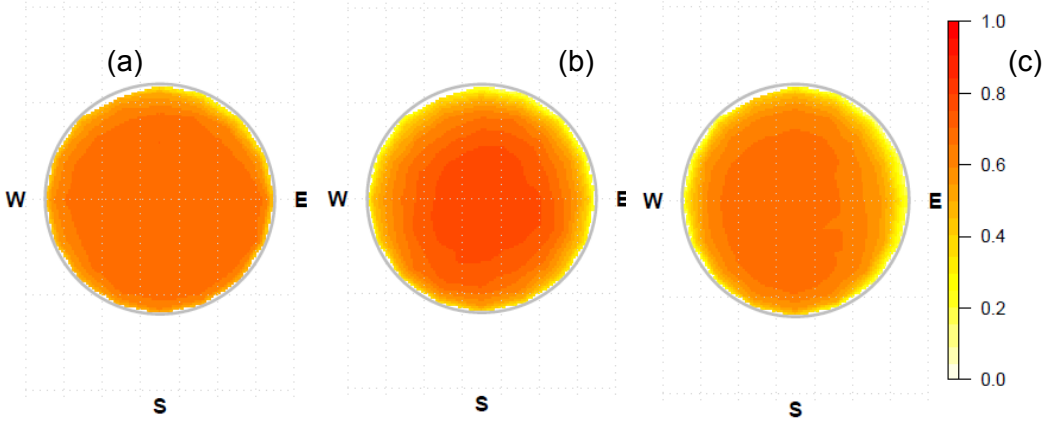

Figure 39: Proportion of viewed shadow by the sensor for (a) R1, (b) R2, and (c) R3 surfaces at (θ_i, Φ_i) = (25°,0°)

5.2.3. Results and conclusion

Spectral data collected with the IFG suggest that there is a large variation of BRF as a function of θ_r and Φ_r. An example is provided in figure 40a-b showing that BRF can vary by a factor 2 under the same illumination conditions.

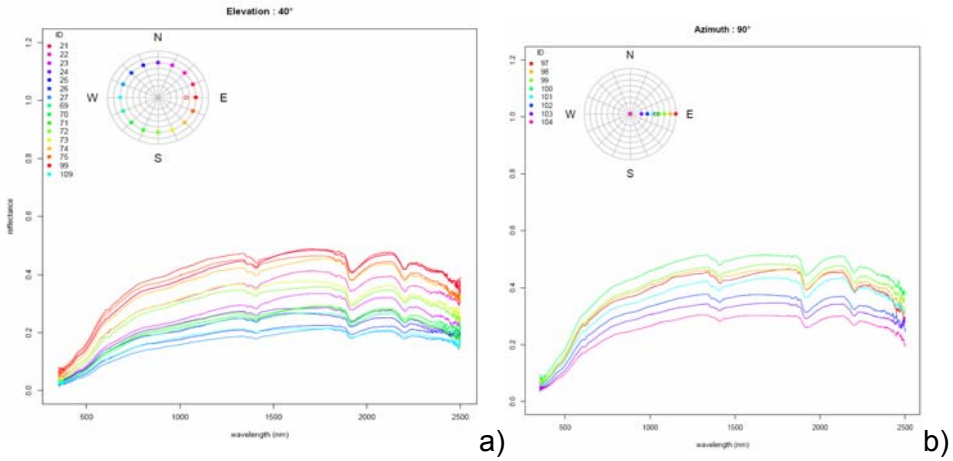

Figure 40: BRF of surface R1 at (θ_i, Φ_i) = (55°,90°) as a function of (a) sensor azimuth (Φ_r) and fixed sensor elevation (θ_r) and (b) sensor elevation and fixed azimuth

The ANIF in the Principal Plane (PP, parallel to the illumination source) shows that it varies as a function of wavelength and that spectral variability is greater between 450 nm and 1400 nm (figure 41a). This corresponds well with what has been observed in an HRS data cube collected in the same area by the AHS-160 sensor. An experimental (image-based) ANIF can be also computed and show indeed a smaller variability at longer wavelengths (figure 41b). Figure 42a-c displays the variation of the ANIF of R1 surface as a function of θ_r, Φ_r, and θ_i. It is clear that the range of ANIF values decreases as θ_i increases. Furthermore, one

can observe a strong backscattering effect (i.e. ANIF > 2 when $\Phi_r \approx \Phi_i$) which decreases with increasing θ_i. The specular component of the scattering (direct reflection at the opposite of Φ_i) seems very low or inexistent. When comparing the different surfaces, R2 shows a slightly larger range of ANIF and also a steeper gradient of values along the PP than R1 (figure 42a-b). R3 has a very steep gradient of ANIF along the PP (figure 42c). This was expected since the ridges are perpendicular to the PP (when $\Phi_i = 90°$) but the figure seems a bit exaggerated due to the small FOV of the spectrometer.

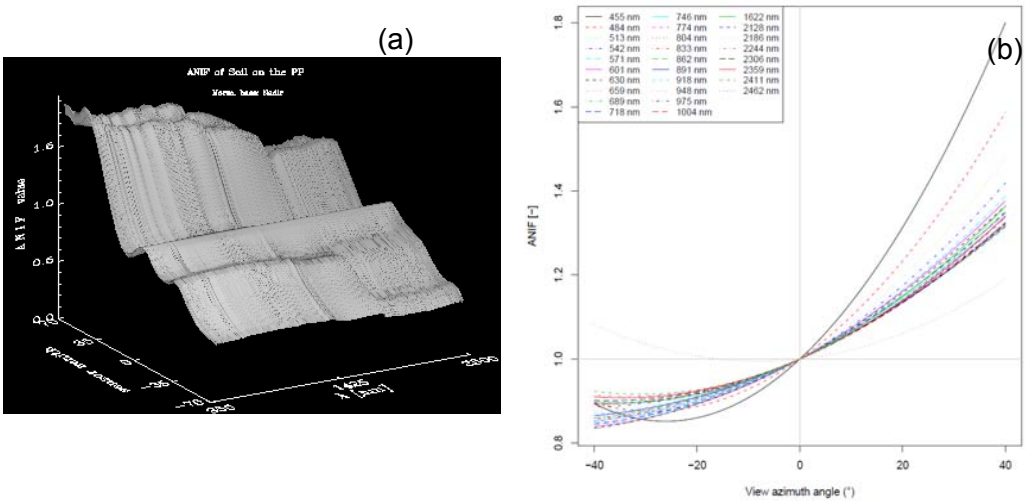

Figure 41: Plots of the ANIF as a function of wavelength and θ_r as computed (a) from laboratory data and (b) image-based HRS data

There is a strong negative correlation between BRF and sensor viewed shadow as shown in figure 43 for the R1 surface. Correlations vary between -0.3 and -0.6. However, there is no clear relationship between the strength of this correlation and θ_i or roughness characteristics of the surface (other figures not shown). This relationship seems also more or less wavelength-independent (figure 43). These results are particularly good considering that viewed shadow has not been directly measured.

Most of the analyses reported here are still qualitative and should be generalized in the future. A meticulous study needs to be carried out in order to (i) quantify the impact of roughness on BRDF and (ii) use the data collected to correct BRDF effects in an existing HRS dataset with the methodology and software developed by Feingersh et al. (2010).

5.2.1. Costs of the experiment and experimental difficulties

The cost in terms of person-day for the laboratory experiment (protocol and experimental setup + spectroscopic and stereoscopic measurements) was about 20 days. The analysis of the data is still ongoing. Using the method and software developed by Feingersh et al. (2010) and spectral data collected in this

experiment, an HRS dataset can be corrected for BRDF-related effects in an automatic way.

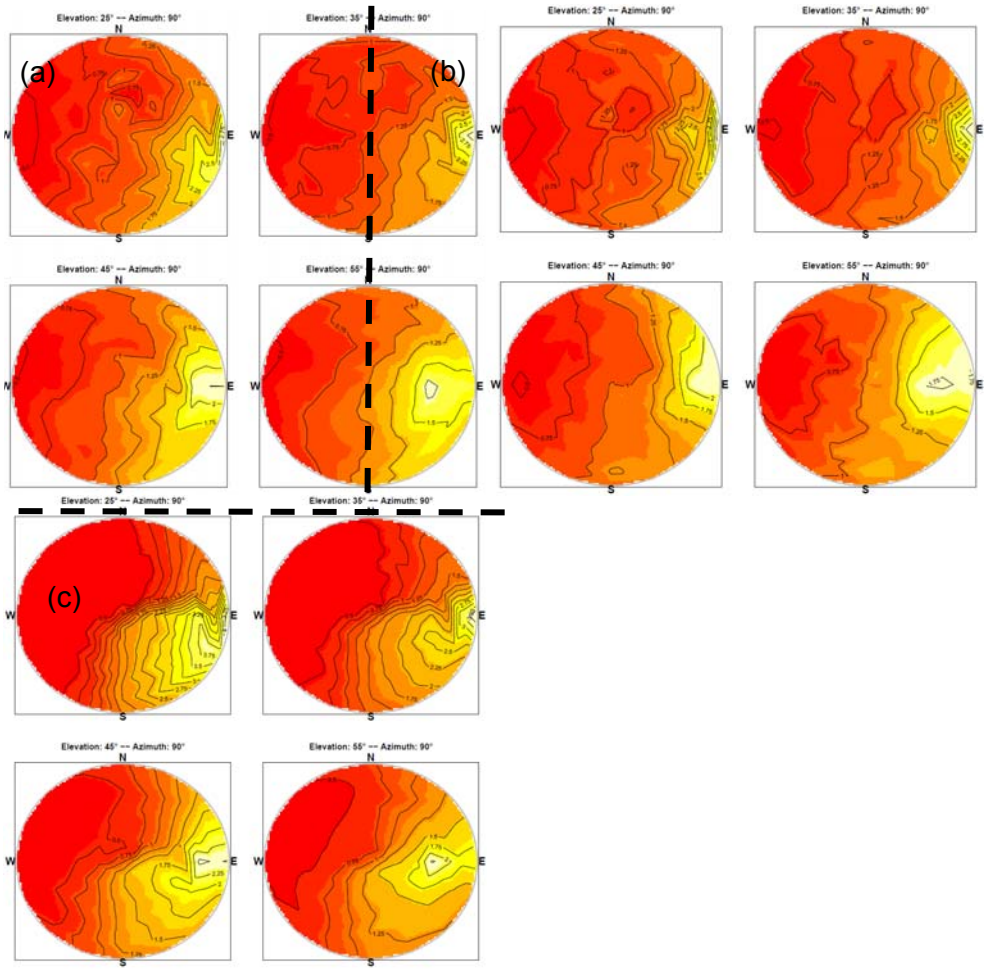

Figure 42: ANIF at 550 nm as a function of θ_r and □$_r$ with □$_i$. = 90° and θ_i = [25°,35°,45°,55°] for (a) R1, (b) R2 and (c) R3 surfaces

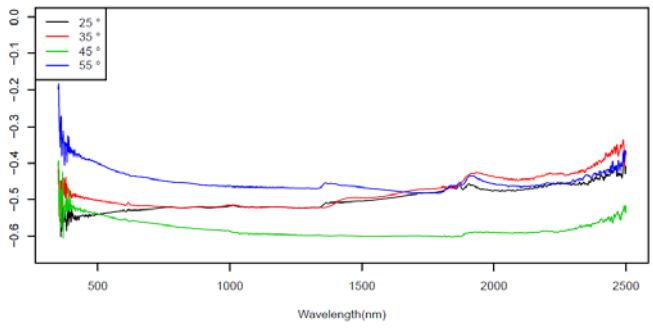

Figure 43: Correlation between BRF and viewed shadow of the R1 surface as a function of wavelength and θ_i

6. Seismic

6.1. SOIL THICKNESS ESTIMATION BY SPECTRAL ANALYSIS OF SURFACE WAVES METHOD AT BOURVILLE SITE

6.1.1. Objectives of the study

Soil erosion is recognised as a major threat through Off-site pollution and muddy floods and its impact on On-site production of biomass, environmental filter and organic matter content. In the European loess belt, soil erosion rates often exceed soil production (figure. 44).

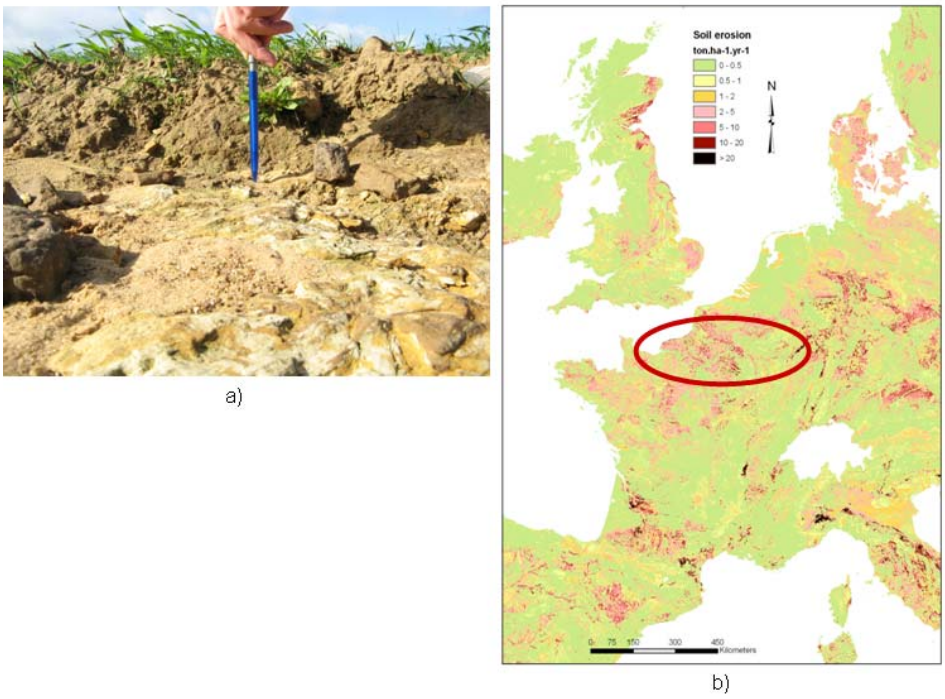

Figure 44: a) Photography showing critical soil thickness; b) Map of soil erosion rates in Europe. The studied area is located in the European loess belt, where soil erosion rate often exceeds soil production (red circle).

As a consequence, a precise spatially characterisation of the soil thickness is required to assess the vulnerability of the soil to different land uses and to investigate its past erosion history. Geophysical methods have been applied to soil sciences for a considerable period. The general principle of geophysical

exploration is to non-intrusively collect data on the medium under investigation. Among such methods, the seismic one is not well established in soil sciences but seems particularly promising because soil properties and physical parameters are strongly correlated and can be quantified through a mechanical aspect. Indeed, the propagation of seismic surface waves in a medium allows to distinguish competent materials (high shear waves velocity) from soft materials like sandstone or unconsolidated rocks (low shear waves velocity). Due to the development of subsurface characterization studied for environmental purposes, the efficiency of seismic methods for estimating ground velocity structures and mechanical properties has been in real progress and has found various applications in the field of waste disposal (Lanz et al., 1998), landslides (Grandjean et al., 2007), or hydrogeophysics (Sturtevant et al., 2004). New equipments with 48 or 72 channels and PC-piloted acquisition software contributed to the development of this method, for example by reducing the acquisition times with unplugged gambled sensors (Grandjean, 2006a). This improvement was also supported by the development of new data processing protocols like acoustical tomography (Azaria et al., 2003; Grandjean, 2006b) or Spectral Analysis of Surface Waves (Park et al., 2000; Grandjean and Bitri, 2006) and its multichannel application MASW (Foti, 2000; Miller, 1999). With the MASW method, we expect to produce at the catchment scale the distribution of Vs along cross sections reaching 0 to 10m deep and to identify the structural configuration of the soil, using horizonation of velocity contrasts with a resolution of several cm. We first present the basic concept of the MASW method and the sensing device adapted to low depth investigation. Then, we discuss the sensitivity of the seismic measurements to the soil stiffness and the retrieval of soil properties and expose the results of the study. Finally, the advantages and limitations of seismic method in soil survey and its application for the assessment of soil vulnerability to erosion is discussed.

6.1.2. Materials and methods

The SASW method is a relatively new in-situ seismic method for determining shear wave velocity profiles. Testing is performed on the ground surface, allowing for less costly measurements than with traditional borehole methods. The basis of the SASW method is the dispersive characteristic of Rayleigh waves when travelling through a layered medium. Rayleigh wave velocity is determined by the material properties (primarily shear wave velocity, but also compression wave velocity and material density) of the subsurface to a depth of approximately 1 to 2 wavelengths. Longer wavelengths penetrate deeper and their velocity is affected by the material properties at greater depth. Four steps are involved in surface waves profiling: (1) field testing for recording surface waves, (2) determination of the experimental dispersion curve from the field data, (3) inversion of Rayleigh waves dispersion from the experimental dispersion curve to obtain a 1D shear waves velocity vertical profile (figure. 45) and (4) interpolation using kriging method to obtain a 2D shear waves velocity section.

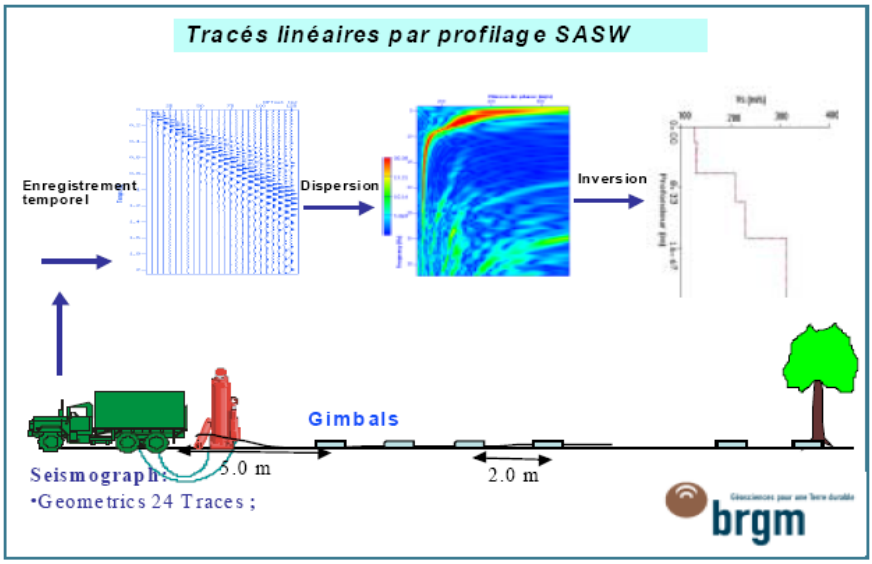

Figure 45: Concept of the MASW method for 1D shear waves velocity profiling

Field configuration and data acquisition

More convenient and better estimation of dispersion curve can be obtained based on a multi-station test configuration (MASW) (figure. 46), in which receivers are located at several locations along a straight line.

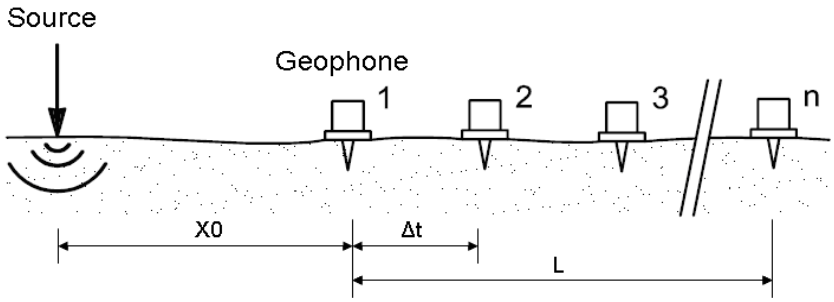

Figure 46: Shematic representation of the MASW device

The wavefield is discretized and truncated in both the time and space domain during the data acquisition. The sampling periods in the time and space domain are Dt and Dx; and the numbers of samples in the time and space domain are M and N; respectively. The near offset x0; geophone spacing Dx; and offset range L are the three important acquisition parameters that need to be properly selected, so as to prevent aliasing, near field, and far field effects. These effects determine the minimum and maximum depth in which VS can be accurately measured by the MASW method. Because of undesirable near-field effects, Rayleigh waves can only be treated as horizontally travelling plane waves after they have propagated a certain distance from the source point. The propagating surface wave may be composed of multiple modes. Identifying individual modes requires

a long offset range (L). Lin et al studied the effects of these acquisition parameters and provide some theoretical guidelines to account for the above concerns. The adaptation of MASW to soil investigation is conditioned by the possibility to reduce the seismic antenna (originally of several tens of meters) to around several meters, in order to get a depth of interest ranging to maximum 10m below the ground surface. This implies to work with very high source frequencies for dealing with high resolution data. We used a small hammer to generate signals in the 1KHz frequency range and a device composed of 24 sensors with a 100Hz main frequency spaced by 50cm towed behind a vehicle (Figure 47).

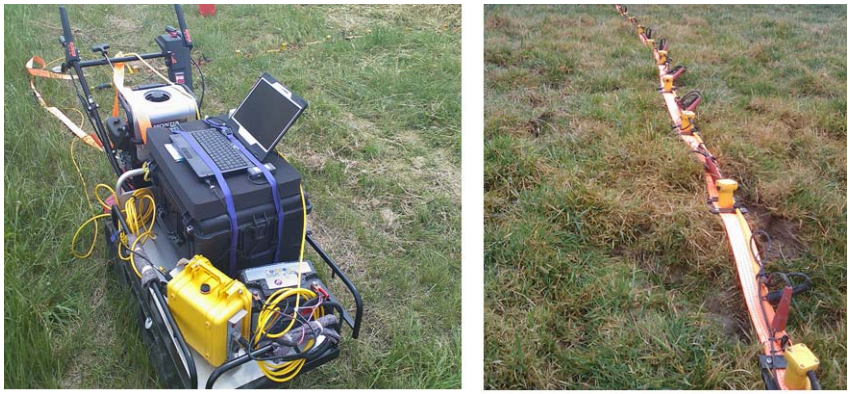

Figure 47: a) Photography of the towing system with the seismic acquisition central; b) Photography of the seismic receivers

3 receivers spacing (10, 20 and 50 cm) have been tested to determine the best device's configuration for spectral analysis of surface waves. The 50cm device appears to be in good agreement with the required objectives in terms of investigation depth and propagation modes identification.

Dispersion analysis

2D wavefield transform method is used to determine experimental dispersion curve. Wavefield transformation methods involve a 2D wavefield transform in which the data are transformed from space–time domain into a more convenient domain. The dispersion curve, i.e., the plot of phase velocity versus wavelength (or frequency), is associated with the peaks in the transformed spectrum. The frequency-slowness (f-p) transform involves first a Radon or t-p transform on the data, followed by a one-dimensional (1D) Fourier transform along the t direction. McMechan and Yedlin (1981) described a technique to obtain phase velocity dispersion from an array of seismic traces, which one is used for this study. They proposed first performing a p-t stack followed by a transformation into the p-ω domain. The Fourier spectrum of a seismic signal at a distance r_n being

$$A(\varpi, r_n)e^{i\phi(\varpi)_n} \quad \text{(eq. 8)}$$

One possible p-ω stack of N traces at different distances from the same source is defined by the relation

$$F(p,\varpi) = \sum_{n=1}^{N} C(\varpi, r_1, r_n)^{-1} A(\varpi, r_n) e^{i\phi_n} e^{i\varpi p r_n} \quad \text{(eq. 9)}$$

Where

$$C(\varpi) = A(\varpi, r_1, r_n)e^{i\phi_1}\sqrt{\frac{r_n}{r_1}}\,. \quad \text{(eq. 10)}$$

Searching for the maxima of

$$\left|F(p,\varpi)\right| \quad \text{(eq. 11)}$$

yields the possible dispersion curves. Since there are N distances, the maximum value of the quantity $\left|F(p,\varpi)\right|$ should be equal to N. In the realistic case of multimode surface waves, (11) will not yield a maximum independent of the amplitude spectrum of the other modes. The stack value will typically be largest for one mode and smaller for others. In the case of a uniform half-space, the dispersion curves extracted from amplitude spectrum in the frequency-velocity domain should exhibit a nearly constant wave velocity with increasing frequency while figure 48a presents a typical shape of dispersion curve performed on a layered medium. The corresponding medium profile is presented in figure 48b. The portions of the curve associated with the sensitivity to the various layers of the medium in figure 48b are illustrated in an approximate way across the top of the dispersion curve. Its general shape justifies the use of receiver spacing of 50cm in combination with 100Hz main frequency sensors as the interesting variation of phase velocity lies at relative high frequency.

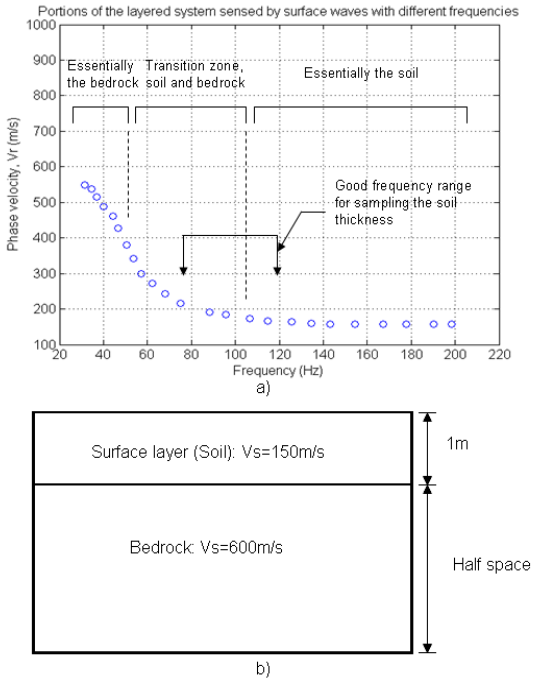

Figure 48: Typical curve from a MASW measurement on the studied area, showing approximate ranges in frequencies associated with sensing different layers of the medium: a) dispersion curve; b) idealized velocity model of the medium

Inversion theory

The inverse problem aims at finding the parameters which characterize in the best way the medium (here the Vs and thicknesses of layers). The real dispersion curves, compared to synthetic curves, create residues of phase velocity, which constitute the *y* data of the inverse problem. The inversion process consists in finding a set of parameters *x* which minimizes these residues in the least square sense. The parameters *x* are linked to the data *y* through a model, which consists in a non linear relation (Tarantola, 1987). This non linear problem can however be linearized to an iterative problem defined by:

$$\left[(Ax-y)^t(Ax-y)+\sigma^2 x^t x\right]=MIN \qquad \text{(eq. 12)}$$

Where A is the matrix of the partial derivatives of phase velocity with regard to the parameters (Vs and thicknesses of layers) and where σ^2 contains the *a priori* information about the model. The matrix A can be decomposed as a function of its values (Λ) and main vectors (U and V) in the following way:

$$A=U\Lambda V^t \qquad \text{(eq. 13)}$$

Then, the solution of the problem by decomposition in singular values is:

$$x = V\left(\Lambda^2 + \sigma^2 I\right)^{-1} \Lambda U^t y \qquad \text{(eq. 14)}$$

The matrix of the *a posteriori* covariance gives an estimation of the trust interval of the model:

$$C = V\left(\Lambda^2 + \sigma^2 I\right)^{-1} \Lambda^2 \left(\Lambda^2 + \sigma^2 I\right)^{-1} V^t \qquad \text{(eq. 15)}$$

In the same way, the resolution matrix is obtained with:

$$R = V\left(\Lambda^2 + \sigma^2 I\right)^{-1} \Lambda^2 V^t \qquad \text{(eq. 16)}$$

A weighting factor *W* was introduced in order to control the variation of the parameters of the model for each iteration. Surf 96 from computer programs in seismology (CPS) is used for data processing (Hermann, 1987).

Retrieval of the soil properties

Some empirical relationships can be found between stiffness and shear wave velocity Vs. We use *in situ* geotechnical parameter qd, which is the dynamic resistance measured with the PANDA penetrometer. Some studies (Gourves and Barjot, 1995) have highlighted correlations between qd and qc obtained from the static penetrometer CPT. On the same way, empirical relations are established between maximum shear modulus Gmax and qc, for various types of soil (Lunne et al., 1997), (Mayne and Rix, 1995). Then we get a good correlation between the stiffness of the material and the shear waves velocity for calibration (figure 49b). The contact with clays is reached at maximum 4m and minimum 50cm for on penetrometric soundings. The qd=15MPa value, which is situated between 200 and 260m/s on the seismic section, is used as a threshold to define the horizon of the boundary between loess material and clays (figure 49a and 49).

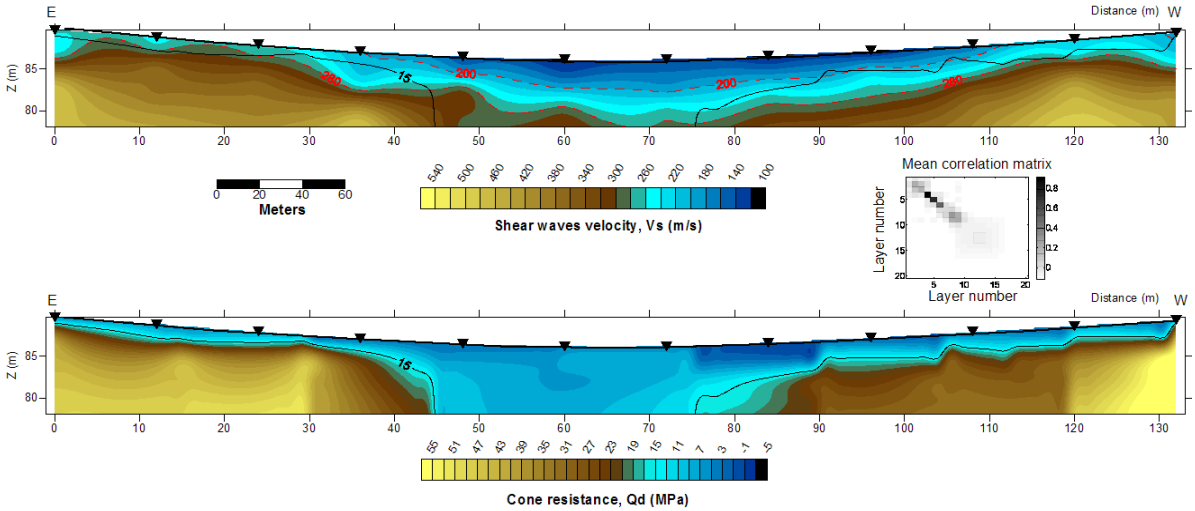

Figure 49: Comparison between Vs and cone resistance sections. The mean correlation matrix indicates that the Vs model is well constrained from ground surface to layer 10 i. e. around 8m depth. The qd=15MPa isovalue is used to calibrate the Vs sections for the horizonation of the contact between loess material and clays. Black triangles represent the positions of both seismic shots and penetrometric soundings along section 5. In the East part of the profile (between waypoint 0m to 30m), the MASW method has no rather good resolution to clearly define the clays horizon at depth lower or equal to 50cm.

6.1.3. Results and conclusion

The studied site is situated in the European loess belt. The white chalk basement is mounted by a layer of clay with flint which is even covered by loess material. The accumulation of loess in the basin is due to a tray's erosion mechanism. We are then expecting strong variations of the soil thickness at the catchment scale. 157 seismic shots were performed along a regular grid with measurements every 12m. 13 sections were investigated in the direction of slopes (profiles 1 to 13) and 3 sections in the transverse direction (profiles 14_T to 16_T). Measurements cover a zone of 140mx150m (2.1 Ha).

A mean velocity value of 240m/s is extracted from the 3D seismic velocities distribution to create an isosurface representing the contact between loess and clays. Then, the soil thickness is obtained, deducting the z value of the Vs=240m/s isosurface at each seismic positions to the z value of the ground surface, given by the topography (figure 50a). Knowing the soil thickness, a mean Vs of loess material over depth is calculated (figure 50b). The map of the soil thickness is coherent with the expected impact of the erosion phenomenon at the catchment scale and presents an asymmetry of the hillsides (loess thickness is lower on the East side than on the West side). Areas of sedimentary accumulation in the basin can easily be distinguished for high loess thickness, whereas zones of reduced loess thickness, associated to a high soil erosion vulnerability are located on the trays. The soil thickness map reveals a local event in the northwest part of the area which is interpreted as an old buried gully

due to preferential streaming in loess material. The low density anomaly, visible at the same location on the bulk density map, corresponds to the filling material of the gully, which has been more recently reshaped (figure 50b). The MASW method offers significant advantages. In contrast to borehole measurements which are point estimates, MASW testing is a global measurement, that is, a much larger volume of the subsurface is sampled. The resulting Vs parameter, obtained from the adapted methodology for soils investigation, is representative of the shallow subsurface stratigraphy and allows an accurate prediction of soil properties averaged over distances. The created maps should be strong inputs for the assessment of soil vulnerability and susceptibility to erosion (and provides indications of historical erosion events) and for problematics of soil compaction controls in cropping systems, shallow landslides detections, or carbon stocks evaluations. The resolution in the near surface is relevant for soil thicknesses more than 50 cm. Because the MASW method is non invasive and non destructive, it is relatively easy to obtain the necessary permits for testing. At sites that are favorable for surface wave propagation, the MASW method allows appreciable cost and time savings. Several other key characteristics of surface waves, give strengths to this application. First and probably foremost is the ease with which surface waves can be generated. The relative high-amplitude nature of surface waves (in comparison to body waves) makes their application in areas with elevated levels of mechanical/acoustic noise possible. A half-space is all that is necessary to propagate surface waves. Surface-wave propagation does not require the velocity to increase with depth and/or a contrast at a boundary (i.e., velocity, density, or combination [acoustic impedance]). Conductivity of soils, electrical noise, conductive structures, and buried utilities represent all significant challenges to electrical or EM methods. These have little or no impact on the generation and propagation and generally no influence on the processing or interpretation of surface-wave data. This flexibility in acquisition and insensitivity to environmental noise allow successful use of shear waves velocity in soils investigations.

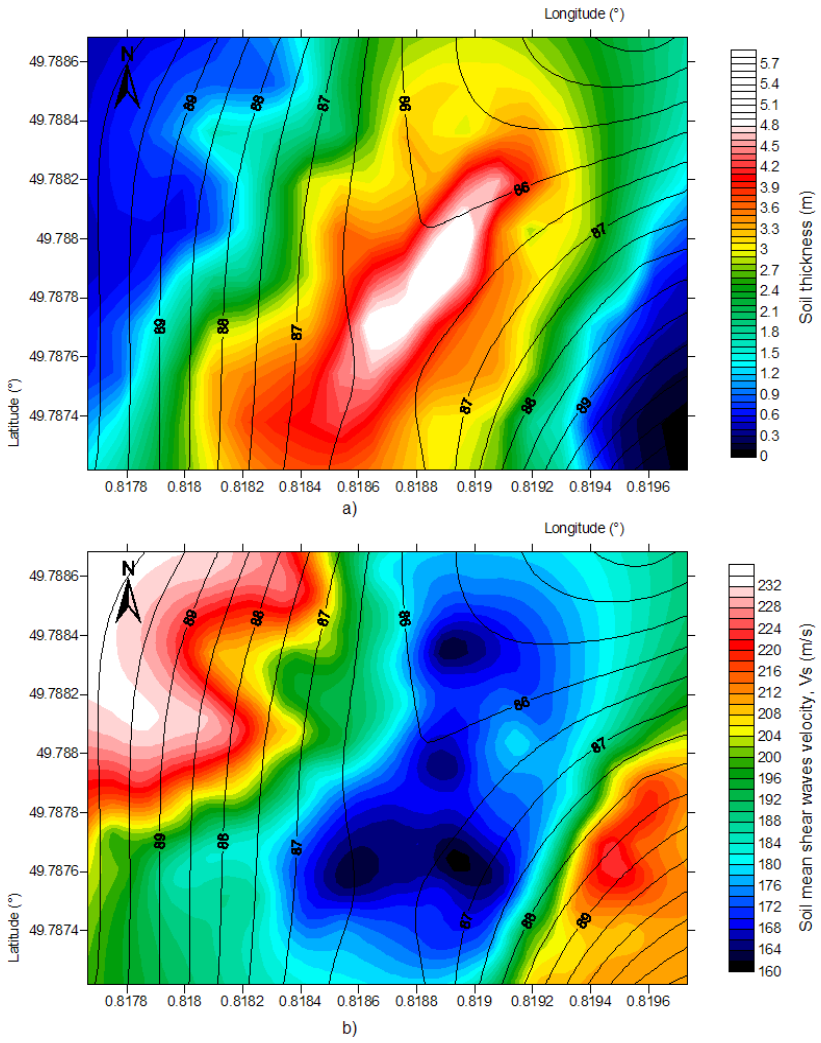

Figure 50: a) map of the soil thickness; b) map of the mean Vs of soil. Most threatened areas in terms of soil erosion are associated to reduced loess thickness. Both maps reveal a local event in the northwest part of the site. Contour lines represent the topography.

6.1.4. Costs of the experiment and experimental difficulties

The cost in terms of person-day for the field experiment (protocol and experimental setup + seismic measurements) was about 5 technicians BRGM days and 5 engineer BRGM days. The processing and analysis of the data was about 10 engineer days using the Surf96 from CPS programs (Hermann, 1987).

6.2. SOIL DEPTH ESTIMATION BY SPECTRAL ANALYSIS OF SURFACE WAVES METHOD COMBINED WITH ERT METHOD AT ROUJAN SITE

6.2.1. Objectives of the study

Soil depth is an important property for estimating crop production potential and soil water availability. Direct estimates of soil depth from destructive boreholes and pits are too costly for being extended to large areas. Geophysical methods are often cited as possible alternative. However their abilities to provide reliable estimations of soil depth are known to be highly dependent on local site characteristics. This study examine the ability of the Spectral Analysis of Surface Waves (SASW) method combined with classical high resolution Electrical Resistivity Tomography (ERT) to predict soil depths in a 500 m ranged Mediterranean hillslope with increasing soil depths along the slope. The toposequence presents shallow groundwater in the lower part and outcrops of an heterogeneous marine Miocene uncemented sandstone with centimetrical laminations in the upper part. This sandstone constitutes the “bedrock”.

6.2.2. Materials and methods

SASW was performed in the field with classical seismic equipment (the same seismic device as the Bourville campaign, composed of a striking hammer and 24 seismic receivers with 10Hz central frequency and 50cm spacing has been used) in June 2009. Data processing was performed using the same method explained in the paragraph 6. 1. 2. At the same place of the seismic profiles, 8 transects of ERT (Wenner-Schlumberger array with 1 meter electrode spacing) were measured in wet conditions (February 2009) and in dry one (August 2009).

Data treatments

Inversion of each section using default parameters of Res2Dinv software (damping factor = 0.5, robust inversion and refinement). In order to calibrate and validate geophysical measurements, observations of 130 boreholes (4 meters deep) were made to determine the soil depths, defined here as the occurrence depth of bedrock. Bedrock was only reached in 35 boreholes, used for calibration of model and cross validation. Figure 51 shows the localisation of performed boreholes, electric and seismic transects.

Figure 51: Position of boreholes (dots), MASW and ERT sections (yellow lines)

6.2.3. Results and conclusion

Firstly ERT and shear wave velocities from inverted SASW were analysed separately. Figure 52 shows that we get a good correlation between the two methods.

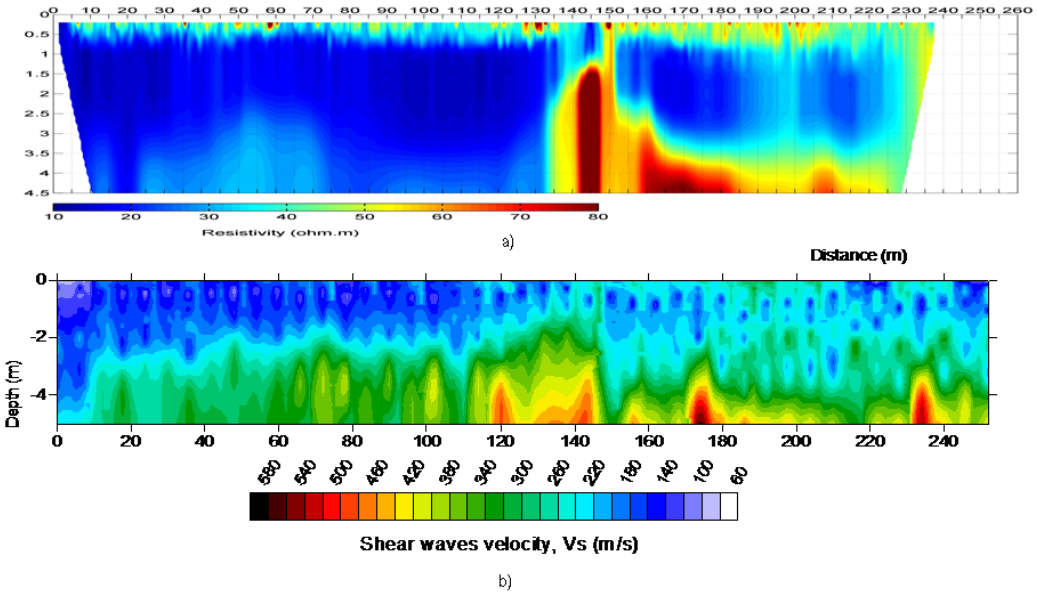

Figure 52: Comparison between a) ERT section and b) MASW section, performed along one of the 8 profiles of the studied area

A statistical analysis of bedrock depth obtained using both geophysical methods and comparison with the real depth obtained from the boreholes, shows that each geophysical method were not sufficient to predict soil depth along the whole hillslope (lower part with calcaric Cambisol / upper part with calcisol). SASW predicted well soil depth in the lower part of the hillslope (with calcaric Cambisol) whereas data from ERT were disrupted by shallow permanent groundwater. Conversely, soil depth was well predicted with ERT in the upper part of the hillslope whereas a high variability of SASW data near the topsoil provided difficulties in soil depth prediction (Figure 53).

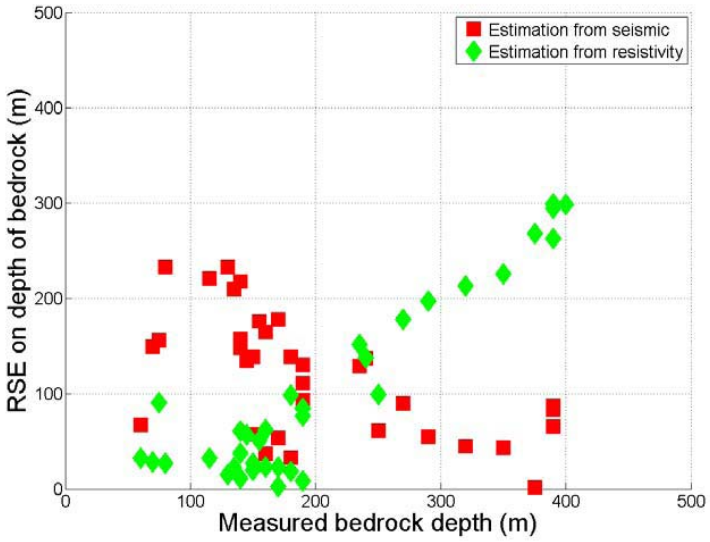

Figure 53: Analysis of RSE of the two methods according to the measured bedrock depth on boreholes

Significant differences in bedrock hardness along the slope explained a part of this high variability. From these results, it was possible to define a new estimator of soil depth that is a weighted mean of the estimations given by each methods, the weights being defined as varying along the slope so that more importance is given to ERT estimates in the upper part of the hillslope and more importance is given to SASW in the lower part (table 8). This study shows the interest of such a fuzzy logic based sensor combination to estimate soil properties when the uncertainty of prediction are variable between locations and geophysical methods.

SE Seismic (m)	SE Resistivity (m)	SE combined (m)
0.1853	5.0702	0.9651
0.6274	0.007	0.0598
2.2798	0.2088	0.3972
0.5393	0.5201	0.5201
NaN	0.0335	0.0335
NaN	8.7007	NaN
0.6211	0.8597	0.3948
3.0394	0.0375	0.0375
1.4147	0.6926	0.6926
0.1293	0.7307	0.7307
0.1899	0.0026	0.0026
1.6523	1.9213	0.3324
4.2721	0.0192	0.0166
3.5986	0.1929	0.1929
0.1445	0.6292	0.6292
0.6315	0.0004	0.0004
3.4902	0.1387	0.1387
NaN	0.0318	0.0318
NaN	9.0595	NaN
2.3535	2.6576	0.9662
2.1334	0.3429	0.3429
2.5834	0.0484	0.0697
1.1912	0.0589	0.0589
2.1054	0.2945	0.2945
1.4816	0.0801	0.0801
0.2942	0.1031	0.1031
0.0056	7.6563	0.0056
3.8659	0.1481	0.0587
7.4338	0.0547	0.0547
NaN	7.4988	NaN
1.9121	3.0016	1.5888
3.996	0.1239	0
1.0496	5.6254	1.8255
0.0165	4.1653	2.674
2.4511	6.7985	2.4511
RMSE 1.36	RMSE 1.39	RMSE 0.7

Table 8: Results of the simulation for the prediction of bedrock depth using the weighted mean estimation method. The obtained RMSE with such combination method is clearly better than using only seismic or electric method.

6.2.4. Costs of the experiment and experimental difficulties

The cost in terms of person-day for the seismic field experiment (protocol and experimental setup + seismic measurements) was about 5 technician- BRGM-days and 5-engineer-BRGM days. The processing of the data was about 10

engineer days using the Surf96 from CPS programs (Hermann, 1987). The analysis of the data is still ongoing with UMR-LISAH Montpellier (France).

7. Conclusion

The present deliverable concerns the second task of the DIGISOIL's WP2. Before their use in real field conditions, the geophysical methods have been tested in controlled conditions, either in the laboratory or in field controlled conditions. This report aimed to present all the experiments conducted and to discuss the ability of geophysical methods to give soil properties. These experiments will comfort the conversion step described in deliverable D2.2, i.e. the assimilation, correction steps realized here on calibration sites. Experiments will be further implemented on validation sites (WorkPackage 3).

Each experiment has been presented classified by each geophysical method: geoelectric, EMI and GPR, magnetism, hyperspectral and seismic. The soil variables of interest were water content, bulk density, clay content and organic carbon content. Variables used for correcting dataset were also obtained as soil roughness. Soil depth and thickness were also estimated, in particular, by seismic method. These soil characteristics will be used in the general processing workflow (see deliverable D2.2) to constrain joint inversion. The soil variables of interest will be then estimated depending on soil layering.

Table 9 presents a synthesis of all the results obtained during this period of calibration tests.

Geophysical tool	Variable of interest	Punctual experiment or temporal monitoring	Nature of the experiment	Site of the studied soil	Soil type	Anciliarry data	Main result
Electrical conductivity (Measurements on cylinders of disturbed soil samples)	Bulk density and water content	Punctual experiment	Laboratory experiment	INRA experimental site of Mons-en-Chaussée (France)	Luvisol	Temperature	Empirical rule between electrical conductivity, water content and bulk density
Electrical conductivity (ECT)	Bulk density	Temporal monitoring (from 15th April and not finished yet)	Field experiment	Beauce site (Villebon, France)	Luvisol	Water content (TDR), bulk density (soil cylinder), temperature (thermometric probes)	Identification of compacted clods and analysis of structural changes intime
Electrical resistivity (ERT)	Geologic structure (lanslides)	Punctual experiment	Field experiment	Telega site (Romania)	Saline soil		Electrical methodology adapted to identify landslides
GPR and EMI	Water content	Temporal monitoring (25 days)	Field experiment	Selhausen site (Germany)	Haplic Luvisol	Water content (TDR)	Map of estimated water content from GPR and EMI signal
GPR	Water content (with the presence of shallow thin layer)	Punctual experiment	Laboratory experiment and field experiment	Center of Belgium (for the field experiment)	Sand (for laboratory experiment) and silt loam (for the field experiment)	Water content (volumetric sampling)	Map of surface soil water content retrieved by two-layered model (first and second layers) from GPR signal
Magnetic viscosity and susceptibility	Carbon content and clay content	Punctual experiment	Laboratory experiment	79 samples chosen in the soil french database	Wide range of soil for different class of clay content and carbon content	Information from the french data base: mineralogy, texture, chemical composition	Trend between magnetic properties and carbon and clay content
Airbone hyperspectral and field spectrometry	Clay content	Punctual experiment	Field experiment	Mugello (Italia)	Ultric and calcereous Regosols, lytic luvisols, humic Umbrisols, anthropic Regosol	SOC, clay minerals, mineralogic composition, iron oxides and CaCO3	Possibility to map total clay content in soils from remotely sensed images
Hyperspectral	Carrbon content	Punctual experiment	Laboratory experiment	Grand Duchy (Luxembourg)	Dystric Regosol, Dystric Cambisols	Soil roughness	Correlation between BRF and sensor viewed shadow. Analysis of BRFD related effect
Seismic: Spectral Analysis of Surfaces Waves (multichannel application)	Soil thickness	Punctual experiment	Field experiment	Bourville (Normandy, France)	Loess material over clay	Dynamic resistance (PANDA Penetrometer)	Map of soil thickness
Seismic/geoelectric: Spectral Analysis of Surfaces Waves combined with ERT	Soil depth	Punctual experiment	Field experiment	Roujan	Calcaric Cambisol and Calcisol	Boreholes	Data fusion method developped

Table 9: General synthesis on all experiments realized on calibration sites

8. References

AKIMA: Interpolation of irregularly spaced data. Fortran code by H. Akima, R port by Albrecht Gebhardt, aspline function by Thomas Petzoldt, enhancements and corrections by Martin Maechler. 2009. R package version 0.5-4. http://CRAN.R-project.org/package=akima

Azaria, A., C. Zelt, A. Levander, 2003. High-resolution seismic mapping at a groundwater contamination site: 3-D traveltime tomography of refraction data, EGS-AGU-EUG Joint Meeting, Nice, France.

Ben-Dor, E., Chabrillat, S., Demattê, J.A.M., Taylor, G.R., Hill, J., Whiting, M.L., Sommer, S. 2009. Using imaging spectroscopy for soil application. Remote Sensing of Environment 113, S38-S55.

Brenning, A. 2010. RSAGA: SAGA Geoprocessing and Terrain Analysis in R. R package version 0.9-6. http://CRAN.R-project.org/package=RSAGA

Cierniewski, J. and Courault, D. 1993. Bidirectional reflectance of bare soil surfaces in the visible and near-infrared range. Remote Sensing Reviews 7: 321-339.

Claerbout, J.F. and Muir, F., 1973. Robust modeling with erratic data. Geophysics, 38, 826-844.

Feingersh, T., Ben-Dor, E. Filin, S. 2010. Correction of reflectance anisotropy: a multi-sensor approach. International Journal of Remote Sensing, 31 : 49-4.

Feingersh, T., Dorigo, W., Richter, R., Ben-Dor, E. 2005. A new model-driven correction factor for BRDF effects in HRS data. EARSeL eProceedings 4, 27-29 April/2005.

Feingersh, T., Schäpfler, R, Ben-Dor, E. 2009. BREFCOR- Towards operational BRDF correction for imaging spectrometry data. Proceedings of the 6th EAESeL Imaging Spectroscopy SIG Workshop, Tel-Aviv, Israel, March 16-18,2009.

Foti, S., (2000) Multistation Methods for Geotechnical Characterization using Surface Waves, Dottorato di Ricerca in Ingegneria Geotecnica.

Gourvès, R., Barjot, R., 1995. Le pénétromètre dynamique léger Panda. Comptes rendus, 11ème congrès Européen de Mécanique des Sols et des Travaux de Fondations, Copenhague, vol. 3, 83-88.

Grandjean G. and Bitri A., (2006) 2M-SASW: inversion of local Rayleigh wave dispersion in laterally heterogeneous subsurfaces: application to Super-Sauze landslide (France). Near Surface Geophysics,, 367-375.

Grandjean G., 2006b. Imaging subsurface objects by seismic P-wave tomography: numerical and experimental validations. Near Surface Geophysics, 275-283.

Grandjean, G., 2006a. A seismic multi-approach method for characterizing contaminated sites. J. Applied Geophys., 58, 87-98.

Grandjean, G., Malet, J.P., Bitri, A., and Meric O., 2007. Geophysical data fusion by fuzzy logic for imaging mechanical behaviour of mudslides. Bull. Soc. Geol. France, 177, 2, 133-143.

Hermann, R.B., 1987. Computer programs in seismology. Saint-Luis University, USA.

Jester W., Klik, A. 2005. Soil surface roughness measurements – methods, applicability and surface representation. Catena 64: 174-192.

Keller, G.V. and Frischknecht, F.C. 1966. Electrical methods in geophysical prospecting. Pergamon Press, Oxford, UK.

Kruse F. A., Raines G. L., Watson K., 1985. Analytical techniques for extracting geologic information from multichannel airborne spectroradiometer and airborne imaging spectrometer data: in Proceedings, International Symposium on Remote Sensing of Environment, Fourth Thematic Conference, "Remote Sensing for Exploration Geology", San Francisco, California, 1-4 April, 1985, p. 309-324.

Kruse F.A., Lefkoff A.B., Boardman J.W., Heidebrecht K.B., Shapiro A.T., Barloon P.J., Goetz A.F.H., 1993. The Spectral Image Processing System (SIPS): Interactive visualization and analysis of imaging spectrometer data. Remote Sensing of Environment, 44, 145–163.

Lanz, E., Mauer, H., Green, A.G., 1998. Refraction tomography over a buried waste disposal site. Geophysics 63, 1414– 2007-02-21.

Ledieu, J., De Ridder, P., De Clercq, P., and Dautrebande, S., 1986. A method of measuring soil moisture by time domain reflectometry. Journal of Hydrology, Vol. 88: 319–328.

Lutterotti L., Bortolotti M., Ischia G., Lonardelli I., Wenk H.-R., 2007. Rietveld texture analysis from diffraction images. Zeitschrift für Kristallographie Supplements, 26, 125-130.

Lutterotti. L. Matthies S., Wenk H.-R., Schults A.J., Richardson Jr., J.W., 1997. Combined texture and structure analysis of deformed limestone from time-of-flight neutron diffraction spectra J. Appl. Phys. 81, 594 (1997); doi:10.1063/1.364220.

Mayne, P. W., Rix, G. J., Correlations between shear wave velocity and cone tip resistance in natural clays, Soil and Foundations 35 (1995) (2), pp. 107–110.

McMechan G. A., Yedlin M. J., 1981, Analysis of dispersive waves by wave field transformation. Geophysics vol. 46 p. 869-874.

Miller, R.D., J. Xia, C.B. Park, J.M. Ivanov. Multichannel analysis of surface waves to map bedrock, SEG 1999.

Nascimento J. M. P., Bioucas Dias J. M., 2005. Vertex Component Analysis: A Fast Algorithm to

Nicodemus, F.E., Richmond, J.C., Hsia, J.J., Ginsberg, I.W., Limperis, T. 1977. Geometrical Considerations and Nomenclature for Reflectance. In: National Bureau of Standards, US Department of Commerce, Washington, D.C. URL: http://physics.nist.gov/Divisions/Div844/facilities/specphoto/pdf/geoConsid.pdf

Otto M., Wegscheiderm W., 1985. Spectrophotpmetric multicomponent analysis applied to trace metal determinations. Analytical Chemistry, 57, 63-69.

Park, C.B., Miller, R.D., Xia, J., Ivanov, J., 2000. Multichannel seismic surface-wave methods for geotechnical applications. Proc. of the First Int. Conf. on the App. of Geophys. Methodologies to Transportation Facilities and Infrastructure, St. Louis, December 11–15.

R Development Core Team. 2009. R: A language and environment for statistical computing. R Foundation for Statistical Computing, Vienna, Austria. ISBN 3-900051-07-0, URL: http://www.R-project.org.

Richard G., Cosenza P., Aboubacar A., Tabbagh A., 2005. Etude des variations de résistivité électrique d'un sol limoneux en fonction de sa teneur en eau et de sa porosité. 5e colloque GEOFCAN «Géophysique des sols et des formations superficielles», 20-21 septembre 2005, Orléans.

Roger-Estrade, J., Richard, G., Caneill, J., Boizard, H., Coquet, Y., Defossez, P., Manichon, H., 2004. Morphological characterisation of soil structure in tilled fields: from a diagnosis method to the modelling of structural changes over time. Soil & Tillage Research, 79, 33-49.

SAGA Development Team, 2008. System for automated geoscientific analyses (SAGA GIS). Germany. URL: http://www.saga-gis.org

Sandmeier S., Müller, C., Hosgood, B., Andreoli, G. 1998. Physical mechanisms in hyperspectral BRDF data of grass and watercress. Remote Sensing of Environment 66:222-233.

Schaepman-Strub, G., Schaepman, M.E., Painter, T.H., Dangel, S., Martonchik, J.V. 2006. Reflectance quantities in optical remote sensing – definitions and case studies. Remote Sensing of Environment 103, 27-42.

Schöpfler, J.T. 2008. Spectrodirectional ground-based remote sensing using dual-view goniometry: field BRF retrieval and assessment of the diffuse irradiance distribution in spectrodirectional field measurements. PhD Thesis University of Zurich, Faculty of Science. URL : http://www.zora.uzh.ch

Shah, P.B., Singh, D.N., 2005. Generalized Archie's Law for estimation of soil electrical conductivity. Journal of ASTM International, Vol. 2(5): 1-20.

Stevens, A., van Wesemael, B., Bartholomeus, H., Rosillon, D., Tychon, B., Ben-Dor, E., 2008. Laboratory, field and airborne spectroscopy for monitoring organic carbon content in agricultural soils. Geoderma 144, 395–404.

Sturtevant, K. A., Baker, G. S., Snyder, C., Kopczynski, S., 2004. Hydrogeophysical characterization of bedrock fracture orientations using azimuthal seismic refraction tomography. AGU, H23A-1122.

Taconet, O., Ciarletti, V. 2007. Estimating soil roughness indices on a ridge-and-furrow surface using stereo photogrammetry. Soil and Tillage Research 93: 64-76.

Tarantola, A., 1987, Inverse problem theory. Elsevier Science Publishing Co., Inc.

Topp, G., Davis, J.L., and Annan, A.P., 1980. Electromagnetic Determination of Soil Water Content: Measurements in Coaxial Transmission Lines. Water Resources Research, Vol. 16: 574-582.

Ufer K., Kleeberg R., Bergmann J., Curtius H., Dohrmann R., 2008. Refining real structure parameters of disordered layer structures within the Rietveld method. Zeitschrift für Kristallographie Supplements, 27, 151-158.

Ufer K., Roth G., Kleeberg R., StanjekI H., Dohrmann R. and Bergmann J., 2004. Description of X-ray powder pattern of turbostratically disordered layer structures with a Rietveld compatible approach. Z. Kristallogr. 219, 519–527.

Unmix Hyperspectral Data. IEEE TRANSACTIONS ON GEOSCIENCE AND REMOTE SENSING, 43 (4), 898-910.

Weihermüller, L., Huisman, J.A., Lambot, S., Herbst, M., and Vereecken, H., 2007. Mapping the spatial variation of soil water content at the field scale with different ground penetrating radar techniques. Journal of Hydrology, Vol. 340: 205-216.

Wold S., Albano C., Dunn W.J., Esbensen K., Hellberg S., Johansson E. and Sjöström M., 1983. Pattern recognition: Finding and using regularities in multivariate data. In: H. Martens and H. Russwurm, Jr., Editors, Food Research and Data Analysis, Applied Science Publishers, London, pp. 147–188.

Wold S., Sjostrom M., Eriksson L., 2001. PLS-regression: a basic tool of chemometrics. Chemom. Intell. Lab. Syst., 58, 109-130.

Zribi, M., Ciarletti, V., Taconet, O., Paillé, J., Boissard, P. 2000. Characterisation of the soil structure and mircowave backscattering based on a numerical three-dimensional surface representation: analysis with a fractional Brownian model. Remote Sensing of Environment 72: 159-169.

Scientific and Technical Centre
RNSC Division
3, avenue Claude-Guillemin - BP 36009
45060 Orléans Cedex 2 – France – Tel.: +33 (0)2 38 64 34 34